

## Article

# Characteristics of Seismogenic Dust Particles from a Mountain and Their Significance for Paleoseismic Records in a Tufa Section: A Case Study of Jiuzhaigou, China

Shengwen Jing<sup>1</sup>, Fudong Wang<sup>1,\*</sup>, Enrico Capezzuoli<sup>2</sup> , Guoqing Huang<sup>1</sup>, Junhao Li<sup>1</sup>, Hanchao Jiang<sup>3</sup>, Zijian Zhou<sup>1</sup>, Xueqin Zhao<sup>1</sup>, Faqin Dong<sup>1</sup> and Andrea Brogi<sup>4</sup> 

<sup>1</sup> School of Environment and Resources, Southwest University of Science and Technology, Mianyang 621010, China

<sup>2</sup> Department of Earth Sciences, University of Florence, 50121 Florence, Italy

<sup>3</sup> State Key Laboratory of Earthquake Dynamics, Institute of Geology, China Earthquake Administration, Beijing 100029, China

<sup>4</sup> Department of Earth and Geoenvironmental Sciences, University of Bari, 70125 Bari, Italy

\* Correspondence: wolfdongswust@163.com



**Citation:** Jing, S.; Wang, F.; Capezzuoli, E.; Huang, G.; Li, J.; Jiang, H.; Zhou, Z.; Zhao, X.; Dong, F.; Brogi, A. Characteristics of Seismogenic Dust Particles from a Mountain and Their Significance for Paleoseismic Records in a Tufa Section: A Case Study of Jiuzhaigou, China. *Minerals* **2023**, *13*, 981. <https://doi.org/10.3390/min13070981>

Academic Editors: Neil M. Ribe, Kaijun Zhang and Xianchun Tang

Received: 16 June 2023

Revised: 5 July 2023

Accepted: 18 July 2023

Published: 24 July 2023



**Copyright:** © 2023 by the authors. Licensee MDPI, Basel, Switzerland. This article is an open access article distributed under the terms and conditions of the Creative Commons Attribution (CC BY) license (<https://creativecommons.org/licenses/by/4.0/>).

**Abstract:** The sedimentary characteristics of the special interlayer contained in the section of the Sparkling Lake dam revealed by the 8 August Jiuzhaigou earthquake in 2017 are obviously different from the tufa in the dam body, and they are considered to be historic flood relics. Based on the study of the particulate matter from the 8 August Jiuzhaigou earthquake, this study combined comparative petrographic, mineralogical, geochemical, and chronological studies of the special interbedded sediments of the Sparkling Lake dam with other genetic samples to obtain homology information and genetic links and to explore the tufa depositional dynamics and earthquake disaster subsidence. The paleoseismic benefit in the discontinuity layer was explored, and the paleoseismic information embedded in the profiles was extracted, providing a new idea for reconstructing the paleoseismic events in the tufa deposition sequence. According to X-ray diffraction, laser particle size analysis, and scanning electron microscope experiments, the particulate matter in the Jiuzhaigou mountains has its own specific mineralogical characteristics. The mineral composition of the particulate matter is basically calcite. The particle size is large, and single particles are mostly angular and subangular. The fracture morphology observed under the single-particle microscope was uneven, showing the characteristics of the dust caused by earthquake disasters. The geochemical analysis data show that the distribution patterns of rare earth elements in different types of particulate matter in the same area have similar characteristics. Moreover, an analysis of the elements Rb, Sr, and Ba shows that the particulate matter in Jiuzhaigou has a strong correlation ( $R^2 = 0.9941$ ), indicating the stability and uniformity of the material source. The source of the particulate matter was limestone of the carbonate strata from the Devonian to the Triassic. Combined with mineralogy and grain size morphology, the interbedded particles in the tufa depositional profile have the potential application of paleoseismic archives to record extreme seismic events. According to the chronological data of the special interlayer sediments in the tufa dam body, the paleoseismic age is inferred to be  $1220 \pm 30$  BP. Therefore, the tufa bedding can be related to the paleoearthquake, and the special interlayer of the tufa section can be used to reconstruct paleoearthquakes.

**Keywords:** Jiuzhaigou; tufa particulate matter; sedimentation; genetic analysis; paleoearthquake

## 1. Introduction

Travertine and tufa refer to the secondary carbonate rocks formed at the surface by the deposition of calcium- and bicarbonate-rich springs, karst water, rivers, and lake systems [1–4]. It mostly developed in the Quaternary period, belonging to typical continental

carbonates or nonmarine carbonates. Travertine is formed from hot water and is hard, crystalline, generally laminated, and a less porous carbonate. Tufa is a cold-water carbonate; it is generally highly porous and contains higher plant and animal remains [2,4–7]. Travertine is gradually regarded as a geological archive of paleohydrology, paleoearthquakes, paleoclimates, active tectonics, glacial processes, plateau uplift and geomorphological evolution, human activities (the Anthropocene), and even the origin of life, owing to the development of its interannual layers, special production background, and biomineralization [8–15], which reveals great potentiality for research.

According to different CO<sub>2</sub> sources in sedimentary water bodies, Pentecost [4] divided freshwater carbonates into two categories: tufa and travertine. The former is caused by atmospheric and soil CO<sub>2</sub> degassing and usually has a low  $\delta^{13}\text{C}$  of  $-12\text{‰}\sim 2\text{‰}$ . The latter is mainly caused by CO<sub>2</sub> degassing from the deep mantle or metamorphic origin, with a high  $\delta^{13}\text{C}$  of  $-1\text{‰}\sim 10\text{‰}$ . Since deep faults in the Earth directly induce or control the recharge, circulation, and uplift of geothermal water, the formation and fracture of travertine is also closely related to faults and seismic activities, and its deposition sites can be used to identify active or potentially dangerous faults and seismic zones. Hancock [16], based on fieldwork on late Quaternary thermogenic travertine in Turkey, the Aegean region of Greece, the Apennine Mountains of northern Italy, and the American basin mountain area, found that travertine can reveal the characteristics and activity history of many neotectonics and, thus, proposed the concept of travitronics. Based on this theory, the dating of travertine produced in tectonically active sites, especially fissure-ridge-type travertine, has allowed for the reconstruction of seismic activity and its repetition [15,17–20], and the assessment of fault spreading rates [21], fault ages [18,22,23], sliding rates [24], and the relationship between faults and fluid properties in geothermal fields have also been studied [25,26]. On the other hand, there have been few cases of paleoearthquakes based on tufa, as the water source is mostly karst water, the concentration of HCO<sub>3</sub><sup>−</sup> is low (<6 mmol/L), and the spring water is not exposed on active faults.

Nevertheless, the tufa deposits that occur in tectonically active areas retain sedimentary abrupt layers (e.g., black peat layers and dirty tufa layers) [27,28] in their sedimentary profiles, which are more likely to be associated with tectonic activity or paleoearthquakes, as tectonic activity alters karst water pathways, or earthquakes cause valley clast debris and phytoclast plant debris to be added to the tufa deposits [29]. The Jiuzhaigou Sparkling Lake tufa profile is a typical case. (1) Jiuzhaigou is located in the north–south seismic belt of China. On 8 August 2017, a 7.0 Ms earthquake occurred, and the mountain debris on both sides of the valley flooded into the water body and triggered the collapse of the Nuorilang Falls and the Sparkling Lake tufa dam break. (2) Guo Yongqiang et al. [27] believe that the dirty tufa layers in the Sparkling Lake tufa are records of flood events, while Lv Congcong et al. [28] believe the formation of the black peat layer is the product of the synergistic effect of many factors caused by strong tectonic activities. These controversies arise from the absence of seismites similar to other sediments or seismically induced sedimentary structures (e.g., liquefaction structures, deformed structures, convoluted structures, and collapse folds) [29] during the deposition of tufa.

Previous studies have proposed that similar historic events may also have exposed fine sediment particles transported by wind to the ancient Diexi Lake by large sandstorms caused by landslides in the Wenchuan earthquake and settled into sediments of nearby lakes. Based on the analysis of rare earth elements (REEs) and the morphology and particle size of quartz particles, it was determined that they originated from 26 seismic events [29–31]. Seismic dust can also be involved in tufa deposition: (1) as in the 8 August Jiuzhaigou earthquake, landslides and collapses in valleys formed a large amount of dust, which was proven by the dust collected on the tourist trestle way in this study; (2) this seismic dust falling into the water body provided nucleation points or templates for tufa precipitation, which is similar to that of biodetritus providing a cushion for calcite nucleation when tufa is deposited; (3) much of this seismic dust was carried by the wind into the river by surface water during heavy rain after the earthquake and participated in

the tufa deposition together with phytoclasts. Based on such an understanding, we assume that the black peat layers and dirty tufa layers in the Sparkling Lake dam are more likely to be the products of earthquake action or that the dust formed by earthquakes is involved in the deposition of these abrupt layers.

This paper compares the mineralogy and particle size analysis of different genetic particles based on sedimentary particles in the abrupt layer of the Jiuzhaigou Sparkling Lake dam, combines the analysis and interpretation of rare earth elements (REEs), establishes the different evolution models of seismic particles in tufa sediments, clarifies how seismic particles in the tectonically active area participate in the process of tufa sedimentation, and presents the paleoseismic information contained in the section with the aim of reconstructing the paleoseismic events in the area. This study provides new methods and thoughts for the study of paleoearthquake recordings on the tufa section in tectonically active areas, and the results can supplement and improve the previous knowledge and theory.

## 2. Geological Setting

Jiuzhaigou is located in Zhangza Town, Jiuzhaigou County, Aba Prefecture, northwest Sichuan Province, 438 km from Chengdu, China, with an altitude of approximately 2000 m to 4750 m and an area of approximately 720 km<sup>2</sup>. Jiuzhaigou is located in the transition zone from a subtropical monsoon climate to a continental plateau climate. It belongs to the warm temperate–middle temperate climate zone of mountain canyons, with obvious vertical zoning characteristics [32]. Geomorphologically, Jiuzhaigou is located in the transition zone between the Qinghai–Tibet Plateau and the Sichuan Basin, which is dominated by alpine mountains and valleys [33,34]. It belongs to the mountainous area of the Baishui River (a tributary of the Yangtze River system) basin and presents an erosional landform landscape that is high in the south and low in the north (Figure 1a), forming a typical alpine valley-type topography with large undulations and height differences. The valley form is a U-shaped valley combined with a V-shaped valley formed by the erosion and incision of glaciers and flowing water. Tufa is mainly distributed in the Shuzhenggou Valley, Rizegou Valley, and Zechawagou Valley, which are Y-shaped, with a total length of 55.5 km (Figure 1c).

Tectonically, the Jiuzhaigou Scenic Area is located at the junction of the Danba–Wenchuan tectonic sheet of the Songpan–Ganze orogenic belt and the Motianling block of the West Qinling orogenic belt [35] (Figure 1b), bounded by the Tazang tectonic belt and the Xueshan and Minjiang faults, with the Motianling nappe of the Western Qinling orogenic belt located in the middle. In the zone, the tectonic process is complex and faults are developed (Figure 1c). A unique NW–SE trending fold structure formed in Jiuzhaigou, and there are four reverse faults in the NW, NNE, NE, and NW. This area has undergone an evolutionary process of 395 Ma, including a marine environment (Devonian~Triassic), orogenic movement (Jurassic~Cretaceous), fault basin (Neogene), Quaternary glaciation (Quaternary), and landscape development (Holocene) [36], and this special geological and tectonic background dominates the stratigraphic spreading characteristics and tectonic development pattern of the scenic area [37]. Identified through a field geological survey and an investigatory report by the Sichuan Bureau of Geology and Mineral Resources, the majority of the outcrops in Jiuzhaigou are marine carbonate formations from the Paleozoic Devonian to the Mesozoic Triassic [38], with the largest outcrop of Carboniferous formations (Figure 1c). These soluble carbonate rocks are widely distributed, and various limestones (including bioclastic limestone, crystalline limestone, argillaceous limestone, and siliceous limestone) and trace amounts of dolomite, slate, and sandstone form the material basis of the Jiuzhaigou karst underground runoff system. The water-bearing medium of the bedrock in the zone is Carboniferous and Permian crystalline limestone, with the best solubility, and the siliceous limestone of the Devonian strata, with relatively poor solubility, forming a karst aquifer, and the metaquartz sandstone of the Devonian and Triassic systems with strong water-insulating properties forming a water-insulating layer.

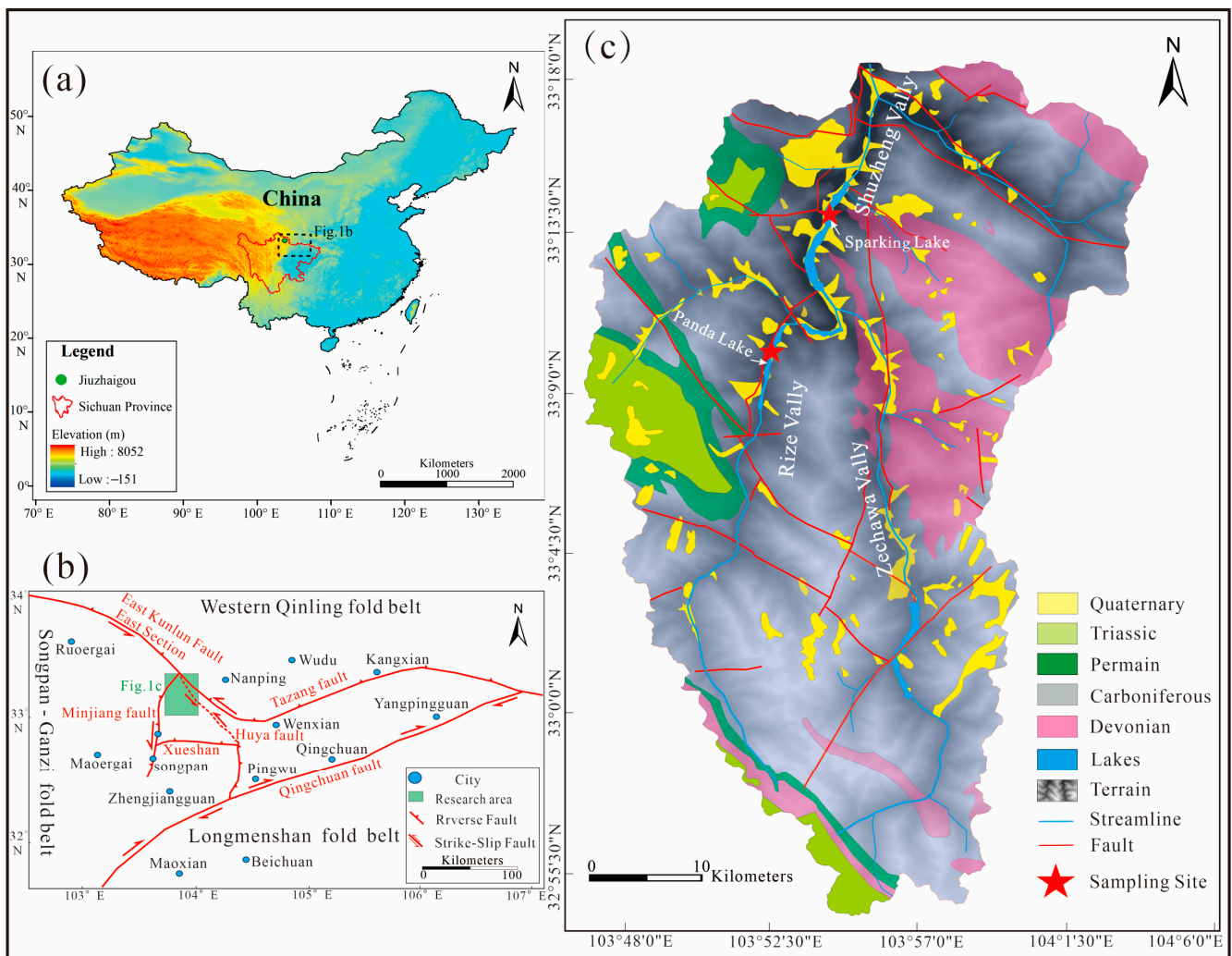


**Figure 1.** Geological background maps of the study area: (a) Map of the location of Jiuzhaigou, northwestern Sichuan Province; the green dots represent the study area. (b) Geotectonic map of Jiuzhaigou; the red dotted line indicates the causative fault of the 8 August 2017 Jiuzhaigou earthquake; the green frame is the area in (c). (c) Geological map of the Jiuzhaigou region [39].

Jiuzhaigou is located on the eastern margin of the Tibetan Plateau [40] and on the thrust fault that transports the Songpan–Ganzi Triassic flysch succession over the Yangtze Paleozoic sedimentary cover [41]. The eastern margin of the Tibetan Plateau involving Jiuzhaigou is impacted by the northeastward extrusion of the Tibetan Plateau due to the continuous subduction of the Indian plate and is marked by strong tectonic activity [42], resulting in frequent earthquakes; the statistical data are shown in Table 1. The earthquakes that have occurred since the 21st century include the 8.0 Ms Wenchuan earthquake in 2008 and the 7.0 Ms Lushan earthquake in 2013. The most recent earthquake was on 8 August 2017, which was a 7.0 Ms earthquake (33.20° N, 103.82° E) that occurred in Jiuzhaigou County [43]. The causative fault is the northern section of the NNW-oriented Hu Ya fault, a left-slip fault that is an important part of the extrusion-transformation tectonic system at the eastern end of the East Kunlun strike-slip fault, absorbing most of the left-slip component of the East Kunlun fault zone [44]. The earthquake caused severe damage to the Jiuzhaigou tufa landscape, resulting in the collapse of the tufa dam body in Sparkling Lake, forming a breach approximately 35 m long and 13 m high, and pouring the lake water out of the dried tufa reef. The seismic dust generated by the earthquake and the outcropping of the dam body provided key samples for the dissection of the tufa sedimentary sequences.

**Table 1.** Typical seismic events in the eastern margin of Qinghai–Tibet Plateau.

Number	Date	Location	Ms	References
1	25 August 1933	Diexi	7.5	[45]
2	14 April 1955	Kangdin	7.5	[46]
3	6 February 1973	Luhuo	7.6	[47]
4	16 August 1976	Songpan	7.2	[48]
5	12 May 2008	Wenchuan	8.0	[49]
6	20 April 2013	Lushan	7.0	[50]
7	8 August 2017	Jiuzhaigou	7.0	[44]

### 3. Sedimentary Characteristics

The study area is located on the northwest side of the Sparkling Lake dam in the Shuzhenggou Valley section of the Jiuzhaigou Scenic Area (33°12′26.04″ N, 103°54′1.62″ E), 100 m away from the scenic road (Figure 2a). Sparkling Lake consists of an arc-shaped dam at the front and a dam at the back, which holds the lake water. A tufa reef (Figure 2a) developed in the lake, with an altitude of 2211 m, length of 232 m, width of 134–294 m, and a storage capacity of 450,000 m<sup>3</sup>.

According to the results of an unmanned aerial vehicle (UAV) survey and field measurements, the vertical height of the levee breach in Sparkling Lake is 13 m (Figure 2a), and it is divided into five layers from the bottom to the top, consisting of three tufa lithofacies: laminated, phytoclastic, and porous biological. The three lithofacies are deposited alternately, with obvious rhythmic sedimentation characteristics. The laminated tufa is a brownish-white sublayer alternating in color (Figure 2b), composed of light and dark dense tufa and characterized by parallel bedding, and a dense tufa layer less than 1 m is often deposited in an inorganic manner due to the action of water flow. The phytoclastic tufa is dark in color, gray and gray-black, containing impurities such as branches and leaves, and the whole layer is messy, superimposed, and fragile, with the thickest part reaching 4 m (Figure 2b). The porous biological tufa is relatively bright in color and formed by algae filaments, mosses, and aquatic plants. Compared to the phytoclastic tufa, its texture is hard, but it is more brittle than the laminated tufa, and the thickest part reaches 5 m (Figure 2b).

A carbonaceous clastic layer, approximately 10~15 cm thick, is interspersed between the phytoclastic tufa and the porous biological tufa in the levee breach, leading to the discontinuity of the tufa deposition. Similar clastic layers are well developed in the rear dam body and tufa reefs in the lake. They are named dirty tufa layers in the tufa reef section (Figure 2c) [27] and are compositionally much higher in carbonate clasts than in carbonaceous. In the rear dam body, they are represented by black peat layers (Figure 2d), and the proportion of carbonaceous and phytoclasts in the material composition is much higher than that of carbonate debris [28]. These rhythmic sedimentary structures and the carbonaceous clastic layer in the dam body provide samples and ideas for the study of historical geological event records and paleoclimate changes.

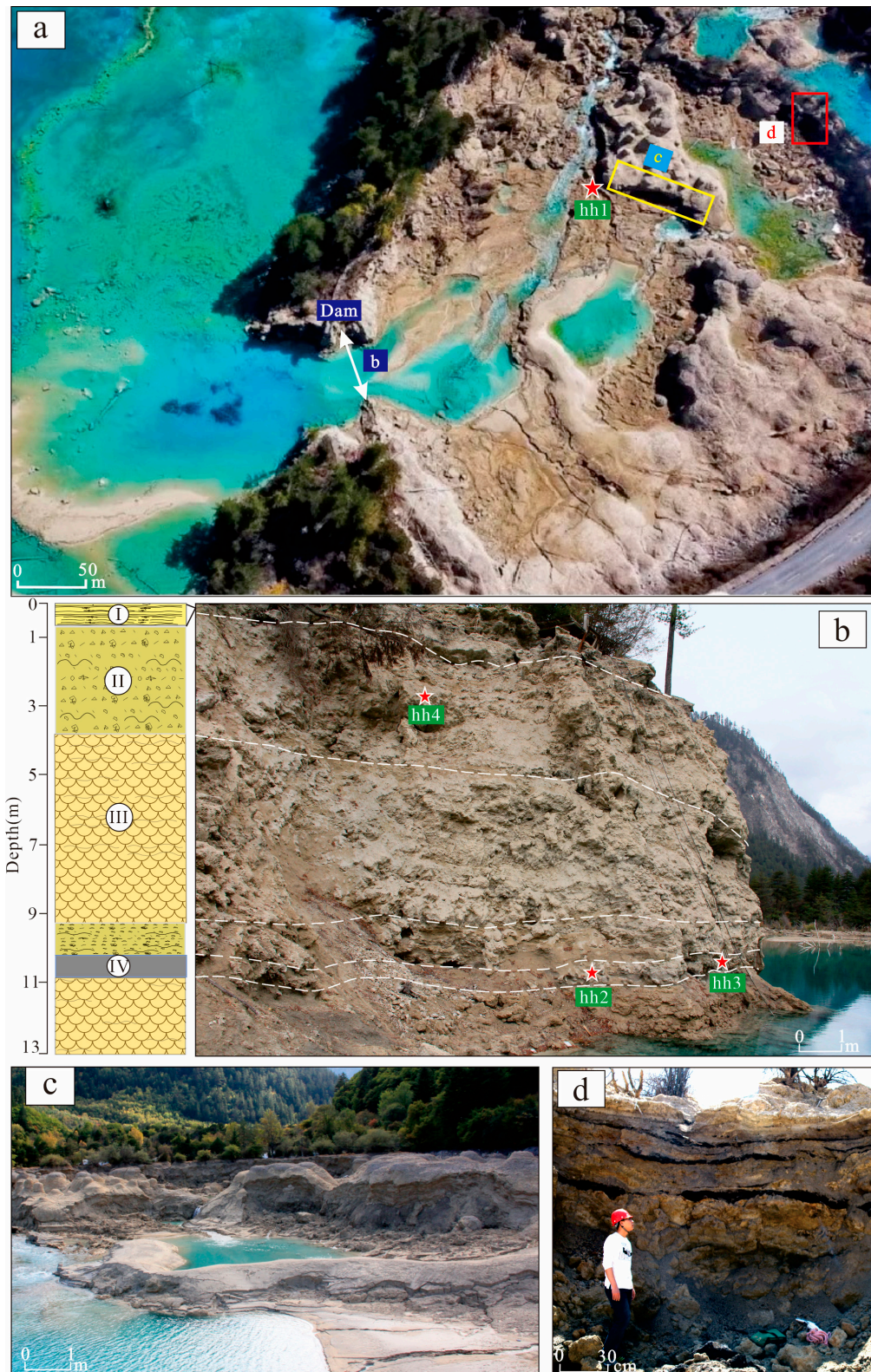


**Figure 2.** Sedimentation characteristics of the Sparkling Lake dam: (a) scene of Sparkling Lake drying up after the earthquake; (b) schematic diagram of the profile of the Sparkling Lake dam, where ★ hh1–4 = chronology sampling sites, I = laminated tufa, II = phytoclastic tufa, III = porous biological tufa, and IV = carbonaceous clastic layer; (c) tufa reef profile in Sparkling Lake [27]; (d) profile of the dam in the rear of Sparkling Lake [28].

#### 4. Materials and Methods

The sampling location is shown in Figure 3. Samples were taken from the settling particulate matter (Figure 3a), fluvial sediments in the lower reaches of Panda Lake (Figure 3b), Sparkling Lake lacustrine sediments (Figure 3c), the special clastic interlayer of the Sparkling Lake dam body (Figure 3d), and collapsed limestone from the mountains on both sides of Panda Lake and Five-Colored Lake in Jiuzhaigou to demonstrate the morphological characteristics of different particulate matter and to reveal the possible material source of the detrital interlayer of the dam body. In order to better identify the eolian sedimentation causes of seismic particles and reveal the paleoseismic information contained in the tufa deposition, Ganzi loess and urban dust were also collected as references.



**Figure 3.** Jiuzhaigou particulate collection location map. (a) trestle way-deposited particulate matter; (b) fluvial sediments in downstream Panda Lake; (c) Sparkling Lake lacustrine sediments; (d) special interlayer sediment of the Sparkling Lake dam body. Yellow arrows indicate sample collection locations.

The mineral compositions of the various samples were determined by an X-ray diffractometer. The instrument model was an XPert PRO. A total of 0.5 g of sample was taken and ground thoroughly, usually to a particle size of 320 mesh, approximately 40  $\mu\text{m}$ . The

powder sample was prepared by the positive pressure method, setting the X-ray diffractor parameters to a 40 kV voltage, 40 mA current,  $0.033^\circ$  step length,  $0.2^\circ$  per minute integration time, and  $3\text{--}80^\circ$  scan range. The compositions of the samples were determined by semiquantitative analysis based on the lower surface reflective intensity of the identified minerals using the weighting factor method.

A laser particle size analysis was carried out using an LS13320 laser particle size analyzer produced by Beckman Coulter Company in Brea, California, USA, and the measuring range of the instrument was  $0.04\text{--}2000\ \mu\text{m}$ . First, a 0.3 g sample was weighed and added to a 200 mL beaker. According to the results of the X-ray diffraction mineral composition analysis, 10 mL of 10%  $\text{H}_2\text{O}_2$  solution was added to the samples with high calcium carbonate content (settling the particulate matter of the dam body, fluvial facies, lacustrine facies, and boardwalk) and heated to fully react with the organic matter. Considering the high content of the organic matter in the samples, when there were still a few bubbles remaining, 10 mL of 10%  $\text{H}_2\text{O}_2$  solution was added again to continue the reaction until no bubbles were generated, at which time the organic matter was completely reacted. For the samples with a high quartz content (Ganzi loess and urban dust), 10 mL of 10%  $\text{H}_2\text{O}_2$  solution was added and heated until only a few bubbles remained according to the pretreatment method of loess particle size analysis. Then, 10 mL of 10% HCL solution was added to remove carbonates and other cements. After cooling, the beaker was filled with deionized water, and after standing still for 12 h, the supernatant was extracted with an eyedropper. Another 10 mL of 0.05 mol/L sodium hexametaphosphate was added to the beaker as a dispersant; then, ultrasonic cleaning and shaking were carried out for 5 min before machine measurement.

Scanning electron microscopy is used to observe the structure, morphology, and other microscopic changes in various minerals. In this experiment, tungsten filament scanning electron microscopy (SEM) was used to analyze the morphology of the individual mineral particles of the samples. The instrument model was an EVO18, and the main accessories included a scanning transmission electron microscope (STEM) and a PP2000T freezing transmission system, and the maximum magnification was  $1,000,000\times$ .

Geochemical element measurement was completed by Guizhou Tongwei Analytical Technology Co., Ltd. in China. The samples were digested with nitric acid, hydrochloric acid, and hydrofluoric acid, which were undergone at least twice at a low temperature and sub-boiling purification by acid purifiers (such as an American Saville DST-1000 and quartz secondary purifier). A high-precision inductively coupled plasma-mass spectrometer (ICP-MS) was used for the experiment. The instrument model was an XSERIES 2. The specific gravity method was adopted for preparing the internal standard solutions of Rh, In, Re, and Bi to control the experimental accuracy. The whole process was carried out at a constant temperature, constant humidity, and in an ultra-clean environment.

The tufa chronology was completed using accelerator mass spectrometry (AMS)  $^{14}\text{C}$  dating at Beta Labs, Miami, FL, USA, with the ages calibrated using IntCal13 curves and BP representing the era to 1950. The dating samples were taken from the upper phytoclastic tufa from the Sparkling Lake breach dam profile, the bottom carbonaceous clastic layer, and the carbonaceous clastic layer extension in the tufa reefs (Figure 2a,b).

## 5. Results

### 5.1. Mineral Phase Results

X-ray diffraction analysis of the mineral compositions was carried out on the detrital interlayer of the tufa dam body in Sparkling Lake, the settling particulate matter and sediments of lake facies of Sparkling Lake, and the fluvial sediments in the lower reaches of Panda Lake and Ganzi loess. The diffraction patterns of the samples were compared and analyzed with the powder diffraction file (PDF) using Materials Data Jade 6.5 software; the results are shown in Figure 4. The mineral composition of the samples in the study area was mainly calcite, among which the compositions of the detrital interlayer of the tufa dam body in Sparkling Lake, lacustrine sediments in Sparkling Lake, and fluvial sediments in Panda

Lake included calcite, quartz, muscovite, kaolinite, and other minerals. A quantitative analysis was carried out using whole peak fitting (WPF) and Rietveld refinement methods to obtain the relative content of each phase, and the results are shown in Table 2.

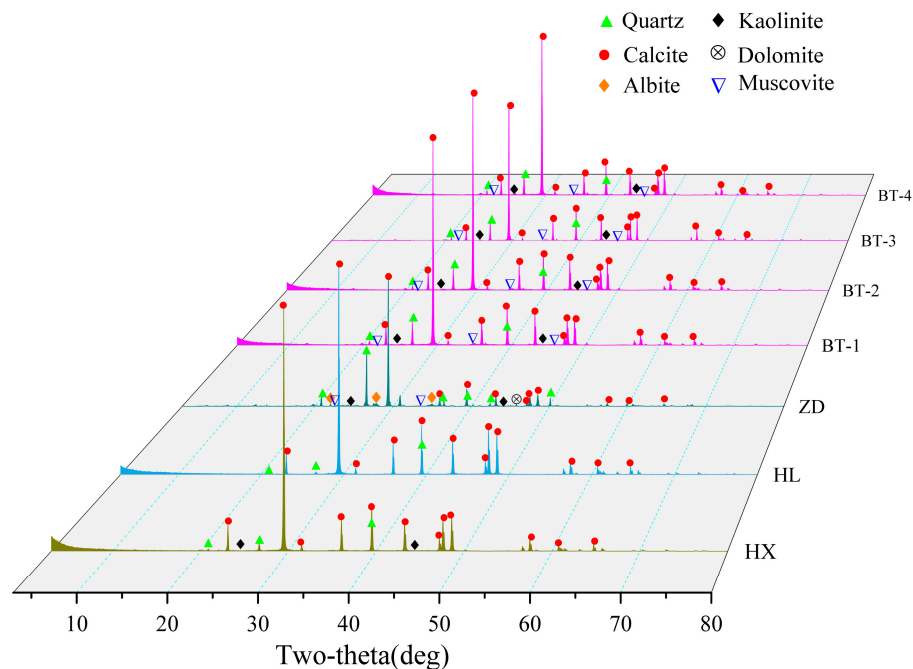


**Figure 4.** X-ray diffraction pattern of the particulate matter in Jiuzhaigou. HX = Sparkling Lake lacustrine sediments; HL = fluvial sediments in downstream Panda Lake; ZD = trestle way-deposited particulate matter; BT = special interlayer sediment of the Sparkling Lake dam body.

**Table 2.** Percentages of the particulate matter minerals in Jiuzhaigou (wt.%). BT = special interlayer sediment of the Sparkling Lake dam body; HX = Sparkling Lake lacustrine sediments; HL = fluvial sediments in downstream Panda Lake; ZD = trestle way-deposited particulate matter; HT = Ganzi loess.

Sample Number	Calcite (%)	Quartz (%)	Muscovite (%)	Kaolinite (%)	Albite (%)	Dolomite (%)	Chlorite (%)
BT-1	79.8	6.2	12.7	1.2	-	-	-
BT-2	80.3	6.3	10.6	2.9	-	-	-
BT-3	77.3	6.9	12.2	3.6	-	-	-
BT-4	78.0	7.4	9.6	4.9	-	-	-
HX	95.1	3.1	-	1.9	-	-	-
HL	98.8	1.2	-	-	-	-	-
ZD	49.7	18.8	13.5	4.3	5.8	7.9	-
HT	1.0	44.2	32.5	4.4	14.7	0.6	2.5

The contents of the mineral components in the detrital interlayers of the Sparkling Lake dam were not much different, and the content of calcite was approximately 80%, followed by muscovite, and the lowest content was kaolinite. The calcite contents in the lacustrine sediments of Sparkling Lake and the fluvial sediments of the lower reaches of Panda Lake were as high as 95%, with a small amount of quartz. The sedimentary particulate matter of the plank was mainly composed of calcite and quartz (Figure 4a). Compared to the lacustrine sediments of Sparkling Lake, the fluvial sediments of downstream Panda Lake, and the detrital interlayer sediments of the dam body, the contents of calcite in the plank settlement particulate matter were significantly reduced to 49.7%, but the content of quartz was significantly increased, and the content of muscovite was equivalent to that

of the special interlayer sediments of the dam body while containing small amounts of kaolinite, albite, and dolomite, whose composition was similar to that of limestone. The mineral composition of the Ganzi loess was mainly quartz and muscovite, the content of calcite was very low at 1%, and other mineral compositions (kaolinite, albite, dolomite, and chlorite) occurred.

In general, the mineral compositions of the samples collected in Jiuzhaigou were generally not very different and clearly distinct from that of eolian loess, but there was an obvious combination with the karst system and fluvial tufa deposition in Jiuzhaigou, and mineral evolution and regional inheritance of the particulate matter in Jiuzhaigou were shown.

### 5.2. Grain Size Distribution

The grain size distribution of sediments refers to the percentages of different-sized grains in the sediment, which is mainly controlled by the transportation medium, transportation manner, sedimentary environment, and other factors. The sedimentary environment and transporting force characteristics of sediments can be studied by grain size analysis [51]. The kurtosis and peak number of the grain size frequency curve can reflect the mode of transport, such as wind and water power, and the grain size corresponding to the thick peak value of the frequency curve reflects the strength of the sedimentary dynamics [52]. The grain sizes of the collected samples were analyzed, and based on this, a discussion of the geological significance of the grain size range of the different samples was conducted, and the sources and geological events were speculated and verified.

As shown in the grain size frequency curve (Figure 5a), the grain size range of the special interlayer sediments in the Sparkling Lake dam body was between 0 and 240  $\mu\text{m}$ , with multiple peaks. The main peak grain size of the special interlayer sediments in the tufa dam was located on the small-ended side, with a concentrated distribution of 2–30  $\mu\text{m}$  and a grain size mode of 6  $\mu\text{m}$ . The kurtosis was sharp, indicating that it experienced good wind transport sorting characteristics. The subpeak grain size was located on the large-ended side, with a grain size distribution of 90–180  $\mu\text{m}$  and a mode of 140  $\mu\text{m}$ . The wide and flat kurtosis indicates poor sorting, displaying hydrodynamic transport characteristics. In addition, there was also a weak peak between 30 and 60  $\mu\text{m}$ . The significant increase in the fine-grained component content in the sediments of the special interlayer of the tufa dam may be related to the large amount of dust or debris materials generated by large-scale landslides and landslides caused by seismic events that were transported to Sparkling Lake and deposited by wind and hydrodynamic forces at a long-term time scale after the earthquake.

As shown in the grain size frequency curve (Figure 5b), the grain size range of the Sparkling Lake lacustrine facies sediments was also between 0 and 240  $\mu\text{m}$ , and the kurtosis distribution of the curve was the same as that of the sediments of the special interlayer of the Sparkling Lake tufa dam body, indicating that they have the same transporting agent and sedimentary background. The difference lies in that the fined-grain component content (2–30  $\mu\text{m}$ ) in the sediments of the Sparkling Lake lacustrine facies was lower than that of the content in sediments of the special interlayer of the dam body, and the kurtosis between 30 and 60  $\mu\text{m}$  was more obvious, indicating that the content of proximal dust increased. On the whole, the Sparkling Lake lacustrine facies sediments are composed of fine-to-coarse silt and fine sand, with the same content of each component and poor grain sorting. They basically correspond to the dust and debris materials produced by the earthquake-induced collapse and landslide that were finally deposited in the Sparkling Lake phase after being transported over a short distance under the synergistic effect of wind and hydrodynamic forces.

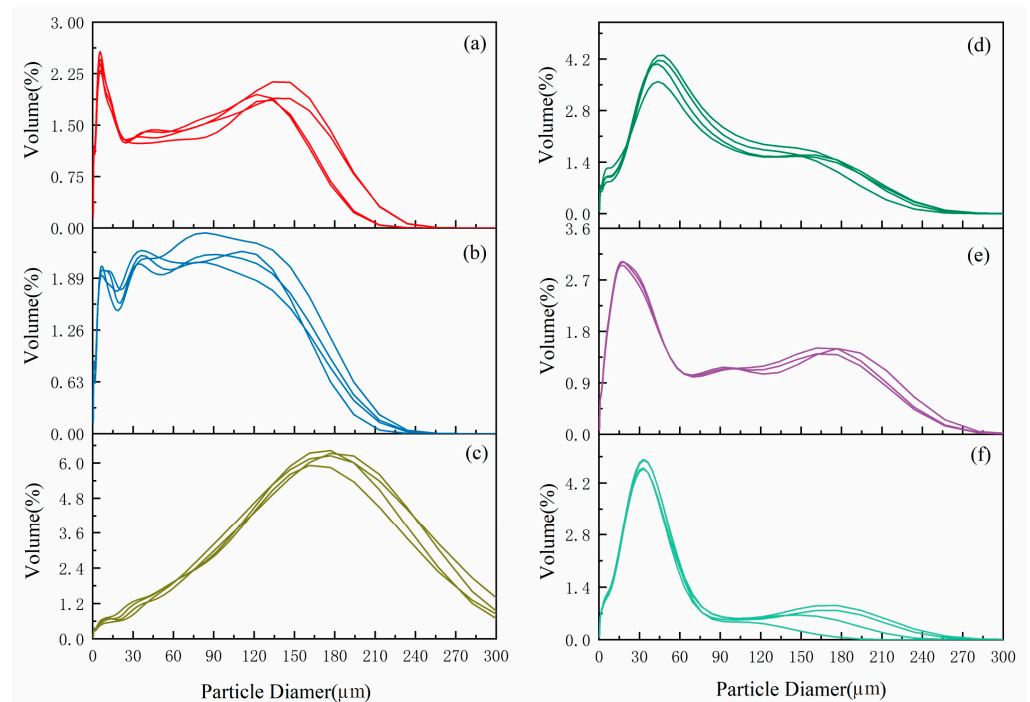


**Figure 5.** Grain size distribution curve of Jiuzhaigou: (a) special interlayer sediment of the Sparkling Lake dam body; (b) Sparkling Lake lacustrine sediments; (c) fluvial sediments in downstream Panda Lake; (d) trestle way-deposited particulate matter; (e) urban dust; (f) Ganzi loess.

The grain size frequency curve (Figure 5c) of the fluvial sediments in the lower reaches of Panda Lake shows a normal fluvial deposition pattern and a generally normal distribution character, with a grain size mainly distributed between 120 and 240  $\mu\text{m}$  and a grain size mode of approximately 180  $\mu\text{m}$ . The grain size is larger than the special interlayer of the tufa dam and lacustrine sediment grains, showing strong hydrodynamic characteristics. There are weak peaks at 7  $\mu\text{m}$  and 30  $\mu\text{m}$ , which are speculated to be dust deposition generated by landslides on both sides of Panda Lake in the river. However, due to the high fluvial energy, only a small amount of dust was deposited into the fluvial facies.

The trestle way grain size frequency curve between Panda Lake and Five-Colored Lake (Figure 5d), the urban dust size frequency curve (Figure 5e), and the Ganzi loess size frequency curve (Figure 5f) all show obvious eolian sedimentary characteristics, and the main peak grain sizes are concentrated at 45  $\mu\text{m}$ , 16  $\mu\text{m}$  and 30  $\mu\text{m}$ , respectively. The main peak grain size of the trestle way grains was significantly larger than that of the urban dust and the Ganzi loess. Studies have shown that grains of size  $>32$   $\mu\text{m}$  are difficult to carry in the air over long-distance transport even under violent wind. The larger main peak grain size indicates the proximal transport attribute [53], and the material source was mainly dust generated by the collapse of the mountains on both sides of Panda Lake. The main peaks of the urban dust and Ganzi loess are sharp and well sorted, which is the result of a strong wind agent and long-distance transport.

### 5.3. Particle Morphology

The morphological analysis of individual mineral particles is of great significance in the restoration process of geological events experienced by particulate matter. The morphological analysis of individual mineral particles under a microscope can well predict the process of evolution [54]. Their sphericity, surface morphology, and other features all contain different geological information.

The X-ray diffraction results show that calcite is the main composition of the special interlayer sediments of the Sparkling Lake dam body, Sparkling Lake lacustrine sediments, and fluvial sediments in the lower reaches of Panda Lake. The sediments of the

Jiuzhaigou trestle way are mainly composed of calcite and quartz, and the loess of Ganzi is mainly composed of quartz and muscovite. The results of the scanning electron microscopy (Figure 6) show that the special interlayer sediments (Figure 6a,b), sediments of the Jiuzhaigou trestle way (Figure 6c,d), Sparkling Lake lacustrine sediments (Figure 6e,f), and Ganzi loess (Figure 6i) had similar surface morphological characteristics. The appearance of the particles was subangular, with no obvious rounded corners, and there was a series of impact craters, fractures, and grooves, suggesting that the particles have the same wind transport characteristics as those in the Ganzi loess (Figure 6i). The impact crater and section were also clear, indicating that the late reformation degree was low in the later stage, and the particles retained their original morphological characteristics, that is, the original particles had experienced sudden and violent impacts with each other, floated in the air for some distance, and settled to the surface, and their material source was the proximal dust generated by earthquake-induced collapse and landslide. The fluvial sediments (Figure 6g,h) in the lower reaches of Panda Lake showed an irregular shape, uneven surface, and higher sphericity, with no obvious impact craters, fractures, or grooves, displaying strong hydrodynamic characteristics. The provenance was weathered detrital tufa deposited after being transported by running water.

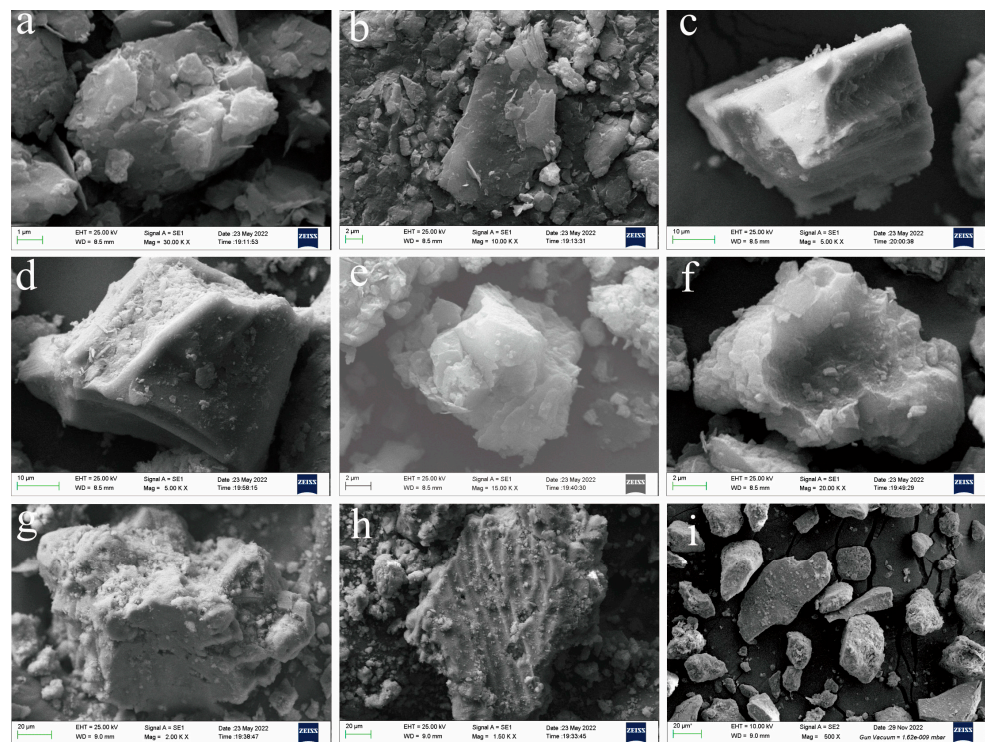


**Figure 6.** Morphology of Jiuzhaigou particulate matter under scanning electron microscopy: (a,b) special interlayer sediment of the Sparkling Lake dam body; (c,d) trestle way-deposited particulate matter; (e,f) Sparkling Lake lacustrine sediments; (g,h) fluvial sediments in downstream Panda Lake; (i) Ganzi loess.

#### 5.4. Composition of Rare Earth Elements

The surface morphology of the particles in Jiuzhaigou is consistent with the inheritance of the study area, as shown by the X-ray diffraction results, and the transport process, as shown by grain size analysis results, over a short distance or time. A rare earth element analysis of the particles collected in Jiuzhaigou was carried out to further demonstrate the stable identity of the provenance and correlation with the earthquake. The analysis results are shown in Table 3. The overall contents of rare earth elements in the Jiuzhaigou particulate matter were relatively low, with a total amount of rare earth elements (excluding Y) that varied from 5.26 to 76.893 ppm and an average value of 35.028 ppm, which was

lower than the average value of the continental upper crust. The contents of light rare earth elements (LREEs) in the study area ranged from 4.26 to 68.69 ppm, with an average of 31.63 ppm, while the abundance of heavy rare earth elements (HREEs) was low, with total contents of 0.7 to 8.20 ppm and an average of 3.39 ppm. The LREE/HREE ratio ranged from 4.29 to 14.87, with an average value of 9.45, which reflects the obvious difference between light and heavy rare earth elements and the characteristics of light rare earth enrichment in the study area. The  $(La/Yb)_N$  values ranged from 6.58 to 21.33, with an average value of 11.61, indicating a distinct difference in the light and heavy rare earth elements. On the premise of chondrite standardization, the  $Eu/Eu^*$  value ranged from 0.58 to 0.66, with an average value of 0.64, which is a moderate negative Eu anomaly. The  $Ce/Ce^*$  value ranged from 0.55 to 1.02, with an average value of 0.96, indicating that the Ce anomaly is not obvious.

**Table 3.** Analysis results of rare earth elements and Rb, Sr, and Ba in Jiuzhaigou particulate matter (ppm). HY = collapsed limestone from mountains on both sides of Panda Lake; HL = fluvial sediments in downstream Panda Lake; HX = Sparkling Lake lacustrine sediments; BT = special interlayer sediment of the Sparkling Lake dam body; ZD = trestle way-deposited particulate matter.  $Eu^*$  is the calculated value at Eu position obtained through linear interpolation based on the content of elements on adjacent sides of Eu;  $Ce^*$  is the calculated value at Ce position obtained through linear interpolation based on the content of elements on adjacent sides of Ce.

Sample	HY-1	HY-2	HY-3	HL-1	HL-2	HX-1	HX-2	BT-1	BT-2	BT-3	BT-4	ZD-1	ZD-2	ZD-3
La	3.38	1.44	2.06	3.42	1.47	3.7	3.74	9.05	9.94	10.4	11.5	15.9	15.8	16.2
Ce	5.38	1.34	4.02	5.09	2.68	7.09	7.23	17.3	19.1	19.9	22	31.3	30.9	32
Pr	0.72	0.25	0.47	0.51	0.31	0.81	0.82	1.99	2.19	2.28	2.51	3.59	3.54	3.66
Nd	2.72	1	1.75	1.67	1.15	2.95	3.01	7.15	7.89	8.21	9.06	13.3	13.3	13.7
Sm	0.528	0.188	0.331	0.24	0.214	0.535	0.557	1.26	1.37	1.42	1.57	2.54	2.53	2.63
Eu	0.107	0.047	0.059	0.047	0.044	0.105	0.108	0.235	0.259	0.267	0.297	0.501	0.484	0.504
Gd	0.529	0.25	0.293	0.202	0.196	0.458	0.467	0.98	1.05	1.09	1.2	2.3	2.22	2.32
Tb	0.08	0.04	0.05	0.03	0.03	0.07	0.07	0.15	0.16	0.17	0.18	0.37	0.352	0.372
Dy	0.477	0.256	0.268	0.191	0.178	0.414	0.407	0.879	0.947	0.973	1.07	2.13	2.05	2.17
Ho	0.1	0.061	0.055	0.041	0.038	0.083	0.082	0.182	0.195	0.198	0.217	0.442	0.419	0.447
Er	0.29	0.18	0.16	0.12	0.11	0.24	0.24	0.54	0.57	0.59	0.64	1.26	1.18	1.27
Tm	0.042	0.027	0.023	0.018	0.018	0.038	0.037	0.085	0.09	0.093	0.101	0.197	0.186	0.195
Yb	0.26	0.16	0.14	0.12	0.11	0.23	0.23	0.55	0.58	0.6	0.65	1.24	1.19	1.24
Lu	0.04	0.02	0.02	0.02	0.02	0.04	0.04	0.08	0.09	0.09	0.1	0.19	0.18	0.185
Y	3.86	3.27	1.81	1.58	1.49	2.47	2.46	5.49	5.79	5.98	6.52	13.4	12.8	13.6
ΣREE	14.65	5.26	9.69	11.71	6.57	16.76	17.037	40.426	44.43	46.279	51.096	75.258	74.331	76.893
LREE	12.84	4.26	8.69	10.97	5.87	15.19	15.47	36.99	40.75	42.48	46.94	67.13	66.55	68.69
HREE	1.81	0.99	1	0.74	0.7	1.57	1.57	3.44	3.68	3.8	4.16	8.13	7.78	8.20
LREE/HREE	7.08	4.29	8.67	14.87	8.37	9.66	9.86	10.75	11.06	11.17	11.29	8.26	8.56	8.38
LaN/YbN	9.4	6.58	10.55	21.33	9.59	11.39	11.66	11.91	12.25	12.39	12.63	9.2	9.5	9.4
Eu/Eu*	0.62	0.66	0.58	0.66	0.65	0.65	0.65	0.65	0.66	0.66	0.66	0.63	0.62	0.62
Ce/Ce*	0.84	0.55	1	0.95	0.97	1.01	1.01	1	1	1	1	1.02	1.01	1.01
Rb	8.39	1.17	1.01	4.34	4.34	11.9	12.0	28.1	32.1	31.3	34.2	56.9	54.6	55.2
Sr	231	818	1290	559	560	647	650	413	436	426	422	328	325.2	317.4
Ba	22	7.85	8.8	31.3	32.5	62.1	62.5	75.3	84	80.5	86.8	212	202	205.6

As can be seen from the chondrite standard curve of rare earth elements (Figure 7), only the limestone and fluvial sediments showed a slight negative Ce anomaly. On the whole, the REE partition patterns of the Jiuzhaigou samples were basically the same, showing an obvious right-inclined pattern. The steep curve in the La-Eu section and gentle curve in the Eu-Lu section show the enrichment of light REEs and a nonobvious fractionation of heavy REEs, and the “valle” characteristics in the Eu area show an obvious negative Eu anomaly. The overall distribution pattern (shape of the partition curve) of all particulate matter in Jiuzhaigou is basically consistent with limestone, and the results of the X-ray diffraction analysis show that the mineral composition of the Jiuzhaigou mountain particulate matter is similar to limestone, which indicates that the provenance of the supply of samples was relatively stable. The collected particulate matter in the Jiuzhaigou mountains originated from limestone, but the rare earth contents of

the samples were different. The general trend of the rare earth contents is as follows: trestle way sedimentary particulate matter > sediment of the special interlayer of the dam body > sediment of Sparkling Lake lacustrine facies > sediment of lacustrine facies in the lower reaches of Panda Lake. The parent rock characteristics and sediment types of the provenance are the main factors affecting the enrichment of rare earth elements [55,56]. Organic matter has the ability to enrich rare earth elements [57], and there are differences in the organic matter contents of different types of sediments. According to the map of the particulate matter collection locations in Jiuzhaigou (Figure 3), it can be observed that the highest organic matter content was found in the deposited particulate matter of the trestle way, followed by the carbonaceous clastic layer sediments of the dam, and the organic matter content was the most important factor affecting the variation in the total rare earth content.

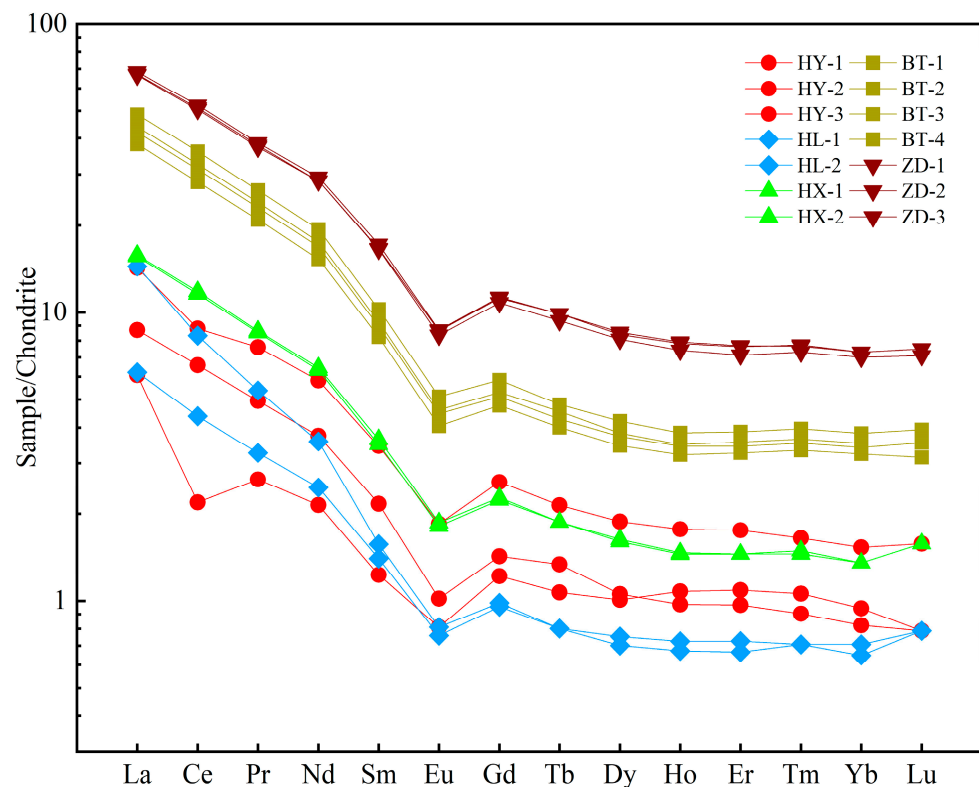


**Figure 7.** Distribution of rare earth elements in Jiuzhaigou by particulate matter. HY = collapsed limestone from mountains on both sides of Panda Lake; HL = fluvial sediments in downstream Panda Lake; HX = Sparkling Lake lacustrine sediments; BT = special interlayer sediment of the Sparkling Lake dam body; ZD = trestle way-deposited particulate matter.

### 5.5. Chronology Analysis

Precise chronological methods to investigate paleogeological catastrophic events are particularly important, and the direct use of carbon flakes to constrain ages in  $^{14}\text{C}$  studies is generally accepted. In this study,  $^{14}\text{C}$  dating was carried out on the phytoclastic tufa and carbonaceous clastic layer at the top and bottom of the Sparkling Lake breach dam profile and the carbonaceous clastic layer in the tufa reefs in the lake, where hh1 in the tufa reefs was deposited at the same level as the carbonaceous clastic layer at the bottom of the dam. The hh1 in the tufa reefs was deposited at the same level as the carbonaceous clastic layers hh2 and hh3 at the bottom of the dam. The results of the sample dating are shown in Table 4, with  $\delta^{13}\text{C}$  values of  $-24.2\text{‰} \sim -26.7\text{‰}$ , which are distinctly different from the epigenetic calcrete  $\delta^{13}\text{C}$  values ( $-12\text{‰} \sim -2\text{‰}$ ) and are typical of the phytoclastic component, making them suitable for  $^{14}\text{C}$  dating. The ages measured for the carbonaceous clastic layer samples hh1, hh2, and hh3 at the base of the dam are consistent within the

error range, with the oldest age being  $1220 \pm 30$  BP and the mean age being  $1190 \pm 30$  BP. The  $^{14}\text{C}$  age of hh4 at the top of the dam is  $350 \pm 30$  BP, which is younger than the ages of hh1, hh2, and hh3 at the base of the dam and is consistent with the tufa depositional sequence from bottom to top, reflecting the reliability and accuracy of the experiment. The  $^{14}\text{C}$  age of the carbonaceous clastic layer allows for an inferred paleoearthquake date of approximately  $1220 \pm 30$  BP. According to the Sichuan Provincial Annals [58], there were multiple severe earthquakes in the northwest of Sichuan Province between 638 and 886 during the Tang Dynasty. The special interlayer of the Sparkling Lake dam may have responded to these historical earthquake events.

**Table 4.**  $^{14}\text{C}$  dating data of tufa in Sparkling Lake dam.

Sample Number	$\delta^{13}\text{C}$ (IRMS, ‰)	Corrected Age (cal BP)	Average Corrected Age (2 $\sigma$ BP)
hh1	−25.3	(412–315 cal BP) (54.1%) (492–420 cal BP) (14.6%)	$1170 \pm 30$
hh2	−26.7	(1182–1050 cal BP) (87.5%) (1030–999 cal BP) (7.2%) (1220–1214 cal BP) (0.7%)	$1180 \pm 30$
hh3	−24.2	(1188–1063 cal BP) (74.5%) (1258–1202 cal BP) (20.9%)	$1220 \pm 30$
hh4	−25.7	(412–315 cal BP) (54.1%) (492–420 cal BP) (41.3%)	$350 \pm 30$

Based on the above experimental results, it was concluded that the mountain particles in Jiuzhaigou were not transported via a long-distance wind agent, the degree of mutual abrasion among the particles was low, and the grain size range was larger than that of eolian particles. Meanwhile, due to the short transport distance, the surface morphology and initial shape of the original particles were still relatively intact after deposition, with lower sphericity and more obvious edges and corners, mostly angular or subangular. In terms of the mineral composition, the Jiuzhaigou mountain particulate matter also bears certain regional inheritance, and the main component is calcite, which is consistent with its geological environment. Most importantly, the contents and distribution of the REEs confirm that the special interlayer of the dam body, fluvial sediments, lacustrine sediments, and trestle way sediments in Jiuzhaigou were derived from the limestone on both sides of Panda Lake. In addition, from the chronology data, it was determined that the special interlayer of the dam formed during a geological event  $1220 \pm 30$  BP.

## 6. Discussion

### 6.1. Sedimentary Model of Seismogenic Dust Particles in Tufa of Jiuzhaigou

Earthquakes cause mountain collapses and landslides, and the clasts form a large amount of dust (even dust storms) while rolling down [59]. These dusts are not transported over long distances and will often settle in close proximity, so mountain slopes or gullies are the main deposition sites. Based on a site survey of the Jiuzhaigou earthquake and a related image survey of the earthquake, this study reconstructed the dust formation of the quake and modeled the formation and deposition process of the seismic mountain particulate matter, taking sedimentary dynamics into consideration (Figure 8).

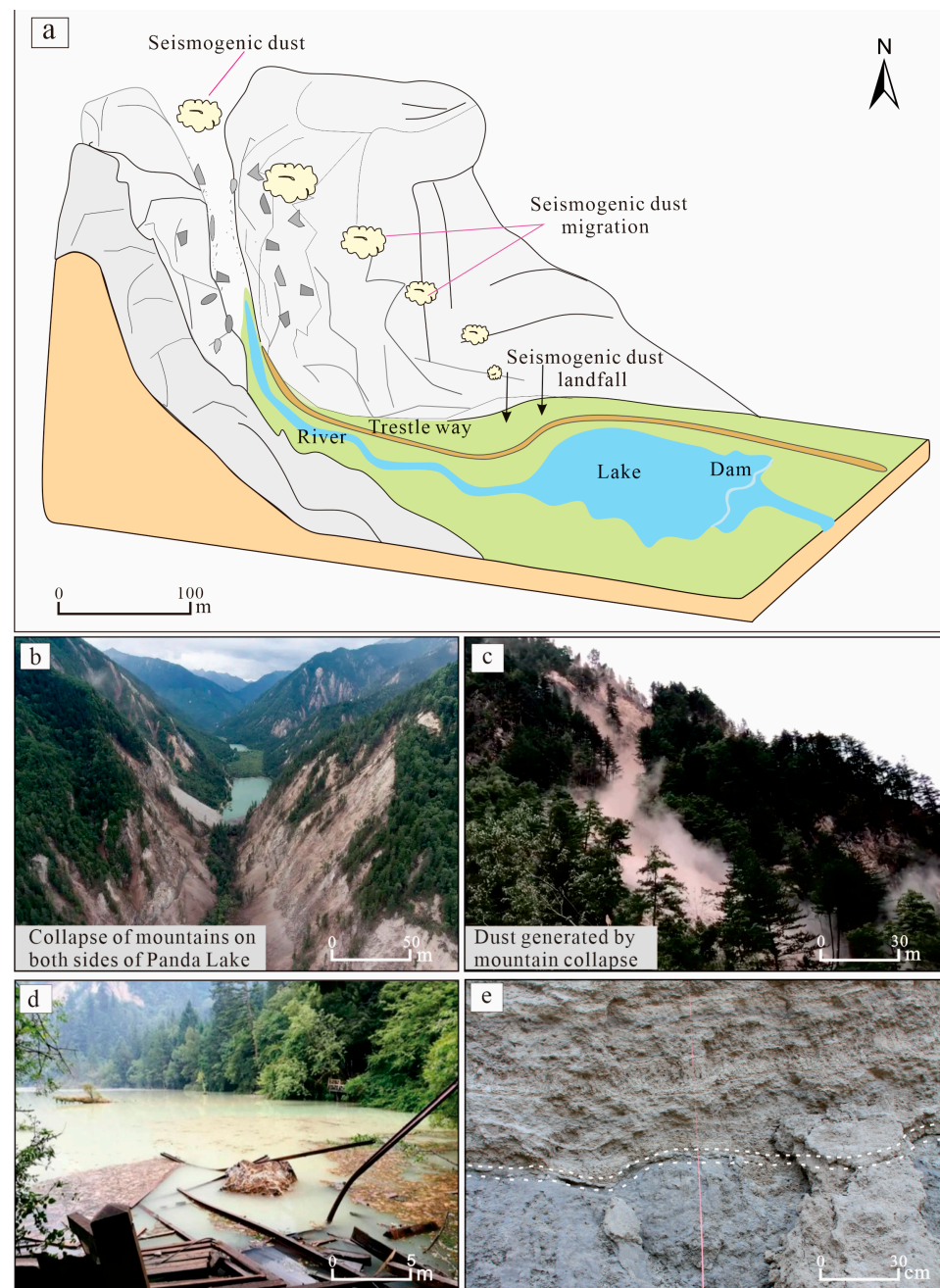


**Figure 8.** Pattern of the particulate matter deposition process in the mountains of the Jiuzhaigou earthquake: (a) seismogenic dust deposition schematic; (b) collapse of mountains on both sides of Panda Lake; (c) collapse of a mountain caused by the earthquake and the generated dust; (d) turbid water caused by particulate matter; (e) special interlayer formed in the dam body of Sparkling Lake.

The earthquake triggered the collapse of mountains on both sides of the front edge of Panda Lake, forming a large amount of mountain dust (Figure 8b,c). Fine dust was suspended in the air for a certain distance and settled on the trestle way between Panda Lake and Five-Colored Lake or on the surface near the collapse area (Figure 8a). Heavy rainfall in a certain time scale after earthquakes (e.g., surface runoff formed by clast flows in the days after the Wenchuan earthquake and Jiuzhaigou earthquake) [60] transported these scattered particles to the river course, and a large number of particles led to a significant increase in water turbidity (Figure 8d). Eventually, these dust or clasts generated by earthquakes were transported by river water and accumulated in the dam body together with phytoclasts

to form a carbonaceous classical layer, as evidenced by the high content of phytoclasts in these layers (Figure 2c) or rich organic matter (Figure 2b,d). For the carbonaceous clastic layer of the Sparkling Lake dam body, its formation mode was the same as the above mode, but the clast source was that of seismogenic dust particles generated in Shuzhenggou Valley in the previous earthquake. The reasons for this are as follows: (1) many collapses and landslides also occurred in the Sparkling Lake and the Shuzhenggou Valley waterfall area (Figure 9a,b) during this earthquake, forming seismogenic dust storms; (2) paleo-collapse and paleo-landslide bodies developed in the Sparkling Lake and Shuzhenggou Valley waterfall area (Figure 9b), which generated seismogenic dust particles from previous earthquakes. Similarly, after sedimentation and post-earthquake rainstorm transport, these clasts accumulated in the Sparkling Lake dam body to form a special discontinuity layer (Figure 8e).

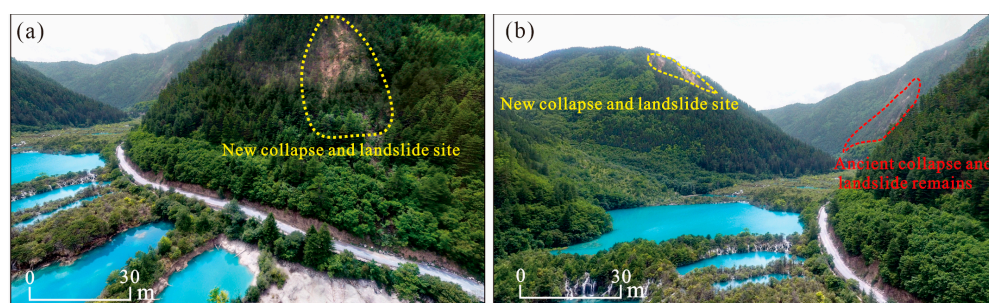


**Figure 9.** Evidence of the collapse of Sparkling Lake: (a) evidence of new collapse and landslide of the mountain on the right side of Sparkling Lake; (b) evidence of mountain collapses and landslides on both sides of the upstream of Sparkling Lake.

From the section of the Sparkling Lake dam body collected from the 8 August earthquake, there was a mode similar to the transport and accretion deposition of detrital particles (Figure 2c,d); that is, when detrital particles were transported to the dam body by the water body, there were carbon dioxide losses due to hydrodynamic changes, and these detritals were similar to the biological residues that provided nucleation sites for calcite crystals [3], forming micrite tufa. Therefore, it was more heterogeneous in mineral composition compared to the lacustrine and fluvial tufas. The quartz content was also relatively high [28] (Figure 4, Table 2). As for the thickness of the carbonaceous classical layer, it was usually less than 20 cm, mostly 5–10 cm, and this thickness was reached because of the mixed phytoclasts. Compared to the normal sedimentary layers of the dam body tufa (laminated tufa, phytoclastic tufa and algae, and moss tufa (Figure 2b), all with a thickness of more than 50 cm), the deposition rate was lower, which can better represent the characteristics of the sedimentary interlayer of geological events.

## 6.2. Paleoseismic Characterization of Morphology and Geochemistry of Mountain Particles

### 6.2.1. Indication of Mineral Composition

According to the X-ray diffraction results, the compositions of the samples collected in Jiuzhaigou were mainly composed of calcite (Figure 4, Table 2), containing a small amount of quartz, which is consistent with the local provenance conditions. According to geological records [61] and field investigation, the composition of the mountains on both sides of the front of Panda Lake is Carboniferous and Triassic limestone with a small amount of sandstone (Figure 1c). The earthquake caused the limestone to collapse, forming limestone clast dust and subsiding near the ground on the trestle way at the foot of the mountain. The sampling location of the particulate matter on the trestle way was just below the collapsed hills on both sides of Panda Lake (Figure 8a,b), and the particle composition is consistent with the mineral composition of limestone. In historic earthquakes, the sedimentary pattern of clastic intercalations in the Sparkling Lake dam body was also as described above. In addition to calcite, quartz accounted for 18.8% of the mineral composition of the trestle sample (ZD)

(Table 2), which is related to the small amount of sandstone interbedded in the mountain stratum. Apart from this, the lowest quartz content in the dam samples (BT) (6.7% on average) was found in the lacustrine (HX) and fluvial samples (HL). The quartz content of the carbonaceous clastic layer was close to that of the seismogenic dust particles, indicating that its origin is related to that of similar seismic particles at the perimeter of Sparkling Lake. The mineralogical composition of the Sparkling lakebed sediments (HX) consisted of calcite precipitated by carbonate supersaturation in the water column due to the inorganic and biological interactions [62]. It also contained a small amount of quartz, which may also be associated with a similar source of seismic particulate matter. Therefore, mineralogical constraints on historic earthquakes can be provided based on the mineralogical composition, combining the geological setting with the sedimentary model of the seismogenic dust particles in tufa and comparing the compositional analysis of the sediments in various depositional environments (e.g., river course, lake bottom, and dam body).

### 6.2.2. Indication of Mineral Grain Size and Morphological Characteristics

Generally, grain size parameters have certain discriminative significance for the genesis and sedimentary environment [63], but in view of the complexity of the sedimentary environment and the diversity of influencing factors, it is usually necessary to conduct a comprehensive analysis of various grain size parameters. According to the size of the detrital particles and the action of the transporting agent, 2  $\mu\text{m}$  and 63  $\mu\text{m}$  were used as the dividing lines of the clay/silt and silt/sand, respectively [64]. A triangulation diagram of the sediment size (Figure 10a) shows that the sediment of the fluvial facies was mainly sand, while the other samples were mainly silt. In terms of the grain size ratio at different levels (Figure 10b), the content of clay was less than 20%. The silt contents of the Sparkling Lake dam body, downstream trestle way of Panda Lake, and Sparkling Lake lacustrine sediment were similar, ranging from 65% to 70%, while that of the urban dust and Ganzi loess were higher than 75%, and the silt content of the fluvial facies was approximately 30% at the lowest level. Moreover, the grain size frequency curve analysis also shows that the fluvial sediments displayed typical fluvial sedimentary characteristics (Figure 5) and strong hydrodynamic transport characteristics. The results of the Panda Lake downstream trestle way, Ganzi loess, and urban dust show obvious wind transport characteristics. The transporting agent of each sediment particle can be explored in accordance with the percentage of the content of silt. The Sparkling Lake dam body, downstream trestle way of Panda Lake, and the lacustrine sediment of Sparkling Lake should have a similar deposition dynamic mechanism, that is, the result of the synergistic effect of wind transport and water transport.

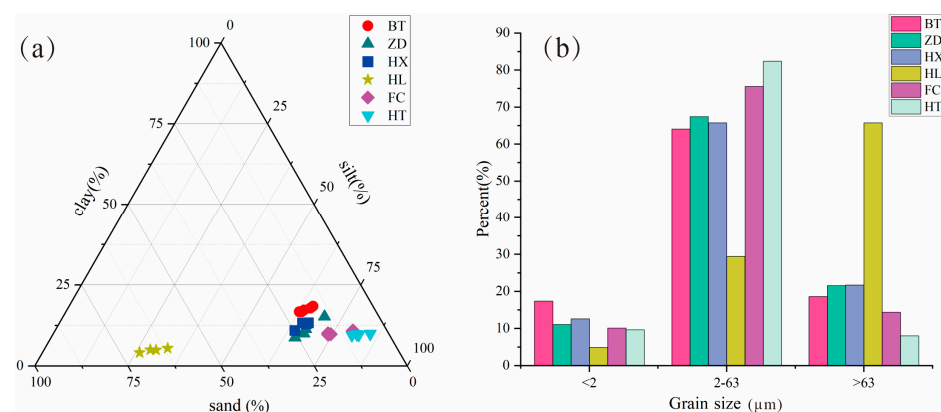


**Figure 10.** Grain size characteristics of Jiuzhaigou: (a) sediment grain size triangle illustration; (b) histogram of the percentage of each grain level. BT = special interlayer sediment of the Sparkling Lake dam body; ZD = trestle way deposited particulate matter; HX = Sparkling Lake lacustrine sediments; HL = fluvial sediments in downstream Panda Lake; FC = urban dust; HT = Ganzi loess.

Research shows that particles of 5~6  $\phi$  (corresponding to 10~50  $\mu\text{m}$ ) float easily in the air and are the main objects for wind suspension transport. As the particle size becomes larger, the transport coefficient becomes smaller, which leads to the weakening of air floating performance. Particles with a size less than 4  $\phi$  (larger than 63  $\mu\text{m}$ ) cannot be suspended in the air and are generally transported by saltation [65]. Through a comprehensive statistical analysis of the sediment grain size parameters, the environmental indexes of different depositional environments and processes can be determined. The discriminant function for identifying the depositional environment ( $Y = -3.5688 \text{Md} + 3.7016 \delta^2 - 2.0766 \text{SK} + 3.1135 \text{Kg}$ , where Md is the median grain size,  $\delta$  is the standard deviation, SK is the skewness, and Kg is the kurtosis) was used to calculate the discriminant values of the Jiuzhaigou particulates and the Ganzi loess (Figure 11). Previous studies have shown that the discriminant function of typical eolian sediments is negative, while most of the aqueous sediments are positive [66,67]. The results of the calculation (Figure 11a) show that the plotting results of the Ganzi loess and urban dust fall in the negative range, indicating the characteristics of wind transport, which is consistent with the actual transporting agent. Fluvial sediment is a typical aqueous sedimentary model, its discriminant value falls in the range of aqueous sedimentation, and the discriminant value reflects the strength of the sedimentary dynamics. Although most of the samples from the Sparkling Lake dam body, lacustrine facies, and trestle way fall in the aqueous sedimentary range, most of them are distributed near the range of a zero-discriminant value, and a small amount of particulate matter from the dam body and trestle way fall in the boundary of sedimentary environments or the eolian sedimentary range. The individual particle results obtained with scanning electron microscopy (Figure 6) show that all the particles in Jiuzhaigou were deposited by close-range transport and had undergone mixed transport of different dynamics, but the original particle characteristics were still retained, in general. These characteristics indicate that the sediment samples at the dam body, the lacustrine facies of Sparkling Lake, and the trestle way are the result of joint transportation by wind and water agents. A scatterplot of the standard deviation of the samples (Figure 11b) and kurtosis (Figure 11c) reflects that the dam body, lacustrine facies, trestle way, urban dust, and Ganzi loess have similar sedimentary environment characteristics, to a certain extent, and are obviously different from those of fluvial sediments.

In conclusion, the proportions of silt content and the discriminant function of the sedimentary environment all intuitively show that the particles of the interlayer of the dam body, lacustrine facies, and trestle way were the result of a combination of wind and aqueous transport. The grain size characteristics of the sediments from the bottom of Sparkling Lake and the interlayer of the dam body were similar to that of the dust or detritus generated by earthquake-induced mountain collapse, which proves that the dust or detritus from an earthquake can be deposited at the lake bottom or accumulate in the dam body after being transported by running water, finally forming a discontinuity layer that is different from conventional hydrodynamic deposition.

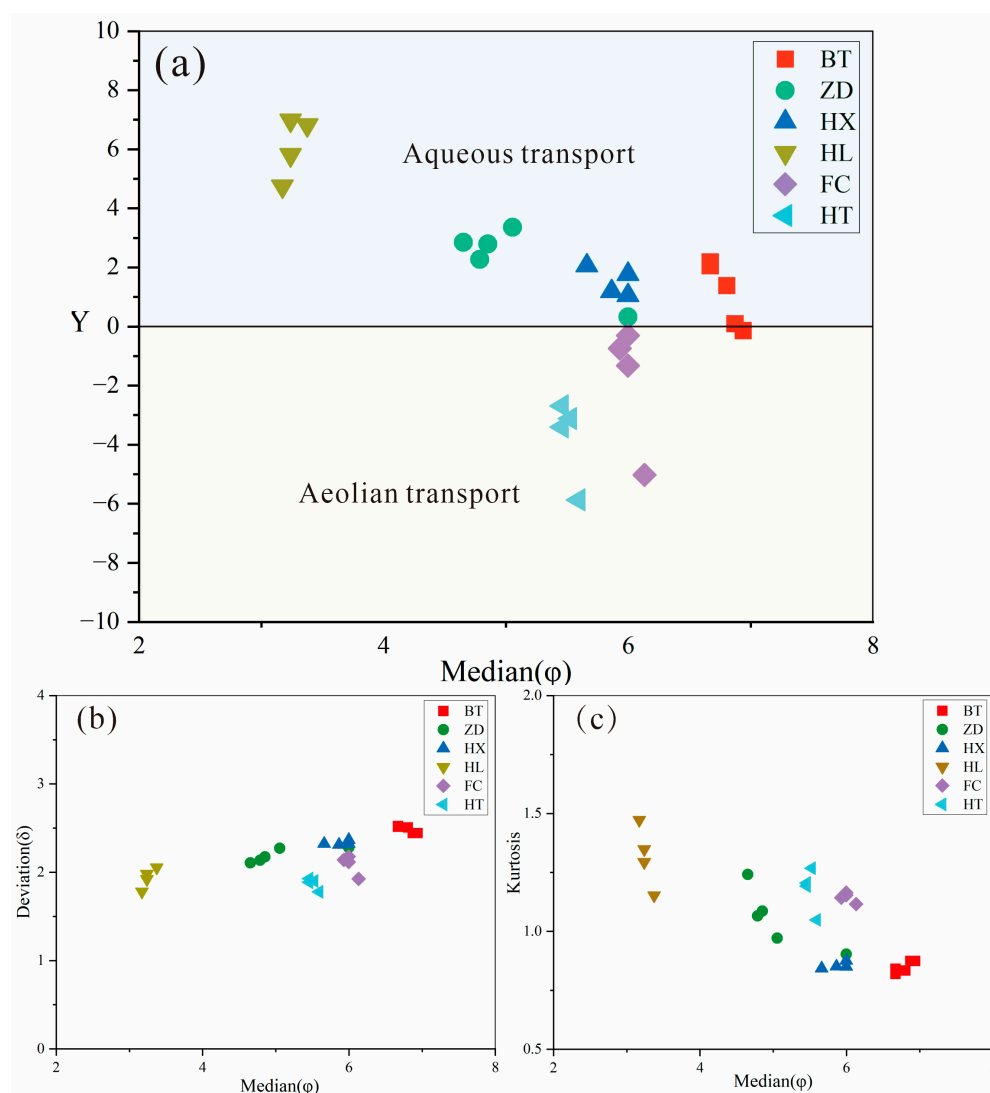


**Figure 11.** Grain size discriminant function diagram: (a) discriminant diagram for different deposition environments of particulate matter; (b) median–standard deviation scatter diagram; (c) median–kurtosis scatter diagram. BT = special interlayer sediment of the Sparkling Lake dam body; ZD = trestle way-deposited particulate matter; HX = Sparkling Lake lacustrine sediments; HL = fluvial sediments in downstream Panda Lake; FC = urban dust; HT = Ganzi loess.

### 6.2.3. Indication of Rare Earth Elements and Rb, Sr, and Ba Composition in Source of Components

Rare earth elements often coexist together in nature due to their similar chemical properties. In the process of external transport, deposition, and metamorphism, the REE compositions and distribution patterns of weathered products experience few changes. Therefore, the REE composition characteristics in sediments are mainly controlled by the source rocks in the provenance area, and rare earth elements are often used as provenance tracers of sediments. The results show that the Eu and Ce depletion and enrichment anomalies of the particulate matter in Jiuzhaigou have strong similarity characteristics. The ratios of  $La_N/Sm_N$  and  $Gd_N/Yb_N$  can reflect the internal differentiation of the sediment LREEs and HREEs. The scatter distributions of the  $Eu/Eu^*$  and  $Ce/Ce^*$  relative LREE/HREE ratios (Figure 12a,b) and  $La_N/Sm_N$  and  $Gd_N/Yb_N$  (Figure 12c) ratios of particulate matter in Jiuzhaigou all display centralized distribution characteristics and are concentrated in the limestone scatter distributions range. This indicates the consistency of the provenance and inheritance of the geochemical characteristics of the regional parent rocks. The relatively small spatial differentiation of the  $Eu/Eu^*$  and  $Ce/Ce^*$  ratios of the particulate matter in

Jiuzhaigou (Figure 13a,b) indicates stable sedimentary environment characteristics, which basically receive no affection from remote provenance. It can be concluded that the interlayer sediment of the Sparkling Lake dam body is mainly from proximal dust or detritus. The overall distribution pattern of rare earth elements is consistent (Figure 7), and the total rare earth content has obvious characteristics of continental margin marine sedimentation [68]. Furthermore, the Rb–Sr–Ba triangle diagram shows the continental margin marine sedimentary characteristics of the limestone (HY), fluvial sediments in the lower reaches of Panda Lake (HL), and lacustrine sediments of Sparkling Lake (HX) (Figure 14a), suggesting that the source of the tufa in Jiuzhaigou was derived from the Devonian–Triassic carbonate strata. Undersaturated karst water is formed after groundwater circulated in these layers. After out-cropping and flowing through different landforms, the tufa was deposited due to the change in the hydrodynamic conditions and the supersaturation of biological action and, therefore, on the whole, it has a consistent pattern of partition. The Sr/Ba–Sr/Rb diagram shows an overall strong correlation ( $R^2 = 0.9941$ ) for particulate matter in Jiuzhaigou (Figure 14b), indicating the stability and homogeneity of the material sources, which are all derived from limestone. A higher correlation ( $R^2 = 0.9947$ ) was found between the trestle way (ZD) and the special interlayer of the Sparkling Lake dam body (BT), suggesting a seismogenic origin for the special interlayer of the Sparkling Lake dam body.

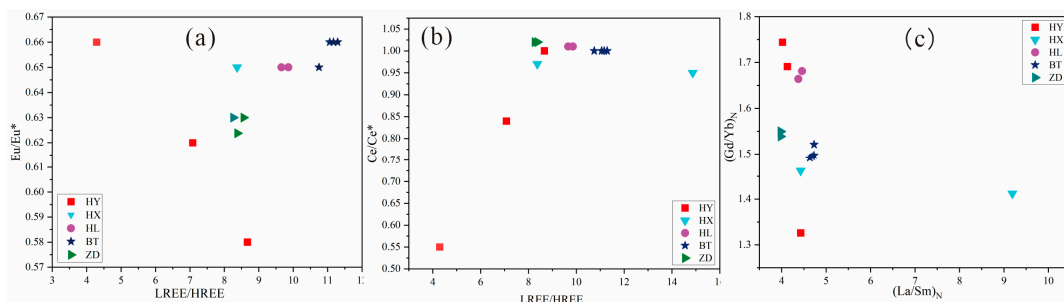


**Figure 12.** Scatter diagram of the characteristic parameters of rare earth elements: (a) Jiuzhaigou particulate matter  $\text{Eu}/\text{Eu}^*$ -LREE/HREE scatter diagram; (b) Jiuzhaigou particulate matter  $\text{Ce}/\text{Ce}^*$ -LREE/HREE scatter diagram; (c) Jiuzhaigou particulate matter  $\text{La}_N/\text{Sm}_N$ - $\text{Gd}_N/\text{Yb}_N$  scatter diagram. HY = collapsed limestone from mountains on both sides of the Panda Lake; HX = Sparkling Lake lacustrine sediments; HL = fluvial sediments in downstream Panda Lake; BT = special interlayer sediment of the Sparkling Lake dam body; ZD = trestle way-deposited particulate matter.

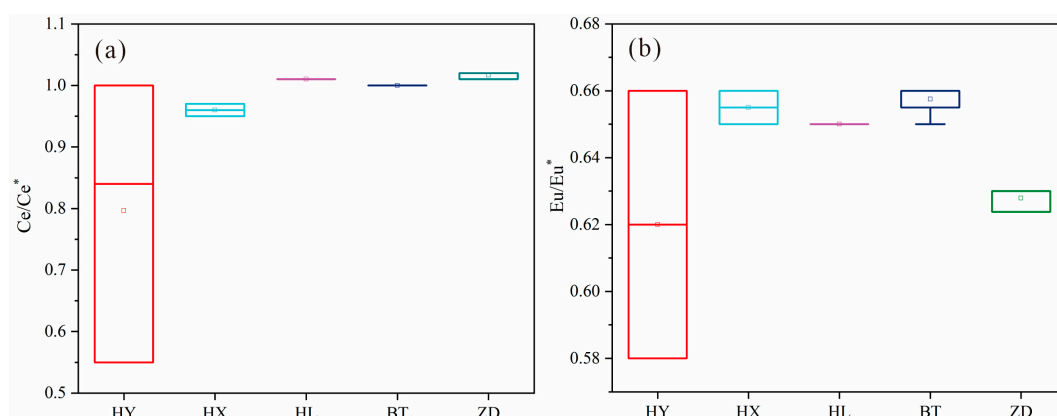


**Figure 13.**  $\text{Eu}/\text{Eu}^*$  and  $\text{Ce}/\text{Ce}^*$  ratios of particulate matter in Jiuzhaigou. (a)  $\text{Ce}/\text{Ce}^*$  ratio of different samples in Jiuzhaigou; (b)  $\text{Eu}/\text{Eu}^*$  ratio of different samples in Jiuzhaigou. HY = collapsed limestone from mountains on both sides of the Panda Lake; HX = Sparkling Lake lacustrine sediments; HL = fluvial sediments in the downstream Panda Lake; BT = special interlayer sediment of the Sparkling Lake dam body; ZD = trestle way-deposited particulate matter.

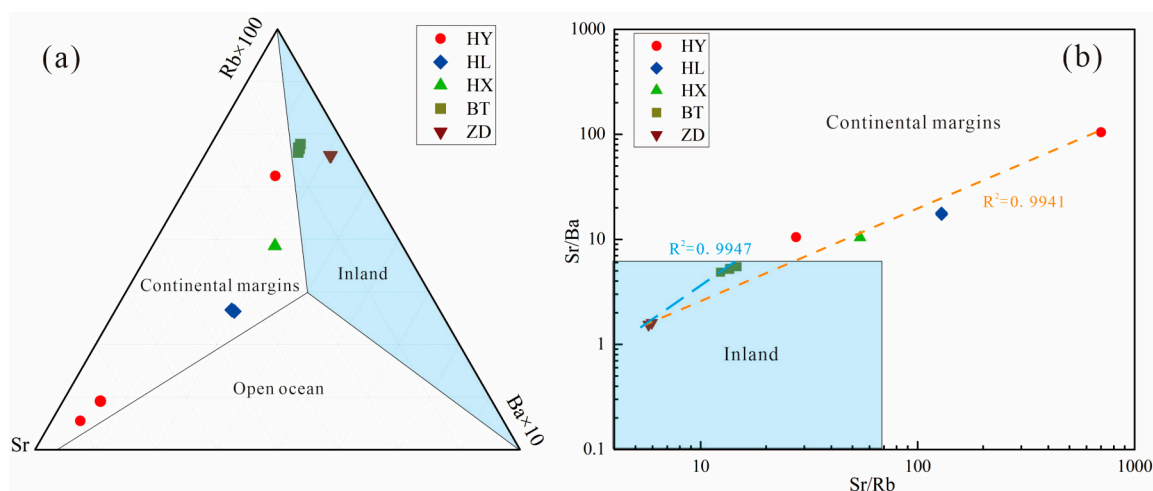


**Figure 14.** Rb, Sr, and Ba indicate the stability of particulate matter sources in Jiuzhaigou, bottom diagram reference from [68]. (a) Rb–Sr–Ba triangle diagram indicative of continental margin marine sedimentary features of limestones. (b) Sr/Ba–Sr/Rb diagram indicates source stability of particulate matter in Jiuzhaigou. HY = collapsed limestone from mountains on both sides of the Panda Lake; HX = Sparkling Lake lacustrine sediments; HL = fluvial sediments in the downstream Panda Lake; BT = special interlayer sediment of the Sparkling Lake dam body; ZD = trestle way-deposited particulate matter.

The total REE content of limestone was relatively low, while that of others was relatively high, which indicates that the secondary carbonate rocks (tufa) may have a greater REE enrichment capacity and are closely related to biological participation (template and respiration). Even though the content of the trestle way particles was the highest, the composition of rare earth elements can reflect a single source of provenance in the same background, and it can well distinguish the specific geological processes of different origins in the same background.

Based on the above results, it can be confirmed that the interlayer sediment of the dam body was of seismic origin rather than fluvial. The specific deposition process was that earthquakes of  $1220 \pm 30$  BP caused geological phenomena such as the collapse of the steep slope on both sides of Sparkling Lake due to historic earthquakes, which caused the dust raised by the collapse to collide violently with each other. Some particles fell to cover the mountain slope and the watercourse, and other particles fell into the water, were carried by the river to be deposited in different places, and then finally deposited in the dam body, showing a special interlayer distinct from the normal flow sedimentary layer. The interlayer of the tufa dam body deposited eventually recorded the corresponding earthquake information, so the study of the tufa sediment profile can reconstruct the paleoearthquake recorded in the dam body.

## 7. Conclusions

The sedimentary characteristics of the special interlayer of Sparkling Lake tufa in Jiuzhaigou are obviously different from those of the conventional sedimentary layer of flows. Through a comparative thinking approach, this paper focused on the comparative petrographic, mineralogical, geochemical, and chronological studies of the interlayered sediments of the dam body and other genetic samples to obtain homologous information and diagenetic links. The paleoseismic benefits of the discontinuity layers in the dam body were also explored by combining the tufa sedimentary dynamics with the subsidence of earthquake disasters, and the paleoseismic information contained in the section was extracted. This paper provides new ideas for reconstructing paleoseismic events in Jiuzhaigou. The main innovative research results are as follows:

1. The mountain particles in Jiuzhaigou have specific mineralogical and petrographic characteristics. According to the results of the X-ray diffraction, laser particle size analysis, and scanning electron microscopy, the mineral composition of the mountain particles in Jiuzhaigou was basically calcite, the particle size was large, single particles were mostly angular or subangular, and the fracture morphology observed under a single-particle microscope was uneven, indicating the dust-lifting characteristics of seismic hazards.
2. The source of the interlayer sediments of the dam body was an earthquake. The tufa sedimentary dynamics analysis shows that seismic particles were transported and deposited near the ground by aeolian formation and accumulated in the tufa dam body by rainfall. The comparative analysis of particle size, morphology, and mineral composition proves the potentiality of seismic particle accumulation in the dam body. The dams in the Rizegou Valley and Shuzhenggou Valley gully systems are characterized by the accretion of particles from the adjacent mountains, as evidenced by the detrital interlayers in the Sparkling Lake dam. All types of particulate matter sources in Jiuzhaigou came from earthquake collapse.
3. Geochemical analysis data indicate that the provenance of various particles in the same area is stable, indicating the homology of the sedimentation of terrestrial carbonate rocks in the karst system. Combined with mineralogy, grain size morphology, and chronology, the interlayer particles in the tufa sedimentary section have the potential to be applied as paleoearthquake archives, and the AMS  $^{14}\text{C}$  age of the black peat layer at the base of the Sparkling Lake dam identifies a seismic extreme event that occurred around  $1220 \pm 30$  BP. Therefore, the earthquake mountain disaster particles in tufa bedding can be linked with paleoearthquakes, and the special interlayers in the tufa section can be used for the reconstruction of paleoearthquakes.

**Author Contributions:** Conceptualization, F.W. and S.J.; methodology, X.Z. and F.D.; software, S.J. and Z.Z.; validation, F.W., S.J. and G.H.; formal analysis, S.J.; investigation, G.H.; resources, F.W.; data curation, S.J.; writing—original draft preparation, S.J.; writing—review and editing, S.J., F.W., E.C. and A.B.; visualization, S.J. and F.W.; supervision, J.L. and G.H.; project administration, F.W. and X.Z.; funding acquisition, F.W. and H.J. All authors have read and agreed to the published version of the manuscript.

**Funding:** This work was supported by the National Natural Science Foundation of China (grant no. 41973053); the Open Fund of State Key Laboratory of Earthquake Dynamics, Institute of Geology, Seismological Bureau of China (grant no. LED2019B05); the Sichuan Province Overseas High-End Talent Introduction Project (grant no. 22RCYJ0060); the Open Fund of Key Laboratory of Mountain Disasters and Surface Processes of China Academy of Sciences (grant no. 19zd3105); the Open Fund of State Key Laboratory of Loess and Quaternary Geology, Institute of Earth Environment, Chinese Academy of Sciences (grant no. SKLLQG1620); the Open Fund of Guangxi Key Science and Technology Innovation Base on Karst Dynamics (grant no. KDL&Guangxi202302).

**Data Availability Statement:** Not applicable.

**Acknowledgments:** We are very grateful to the Jiuzhaigou Administration for their support and assistance in the field work to ensure the smooth conduct of the study, to Guizhou Tongwei Test Technology Co., Ltd. for the accurate analysis of the rare earth elements, and to Yunzhou Xu, Jiachuan Yu, and Congcong Lv for their valuable comments during the writing of the paper. Many thanks to the academic editors and the three peer reviewers for their constructive suggestions to improve the quality of the article.

**Conflicts of Interest:** The authors declare no conflict of interest.

## References

1. Ford, T.D.; Pedley, H.M. A review of tufa and travertine deposits of the world. *Earth Sci. Rev.* **1996**, *41*, 117–175. [[CrossRef](#)]
2. Pedley, H.M. Classification and environmental models of cool freshwater tufas. *Sediment. Geol.* **1990**, *68*, 143–154. [[CrossRef](#)]
3. Wang, F.; Zhao, X.; Dong, F.; Capezzuoli, E.; Malov, A.; Du, J. Classification of Alpine-type travertine in Jiuzhaigou valley on the eastern margin of the Qinghai-Tibet Plateau. *Carsologica Sin.* **2021**, *40*, 112–124.

4. Pentecost, A. *Travertine*; Springer Science & Business Media: Berlin, France, 2005; pp. 1–445.
5. Enrico, C.; Anna, G.; Martyn, P. Decoding tufa and travertine (fresh water carbonates) in the sedimentary record: The state of the art. *Sedimentology* **2014**, *61*, 1–21.
6. Karaisaoğlu, S.; Orhan, H. Sedimentology and geochemistry of the Kavakköy Travertine (Konya, central Turkey). *Carbonate Evaporite* **2018**, *33*, 783–800. [[CrossRef](#)]
7. Koşun, E. Facies characteristics and depositional environments of Quaternary tufa deposits, Antalya, SW Turkey. *Carbonate Evaporite* **2012**, *27*, 269–289. [[CrossRef](#)]
8. Andrea, S.; Paola, M.; Michele, S.; Paola, T.; Erlisiana, A.; Andrea, B.; Stefania, F. The uplift of the Adriatic flank of the Apennines since the Middle Pleistocene: New insights from the Tronto River basin and the Acquasanta Terme Travertine (central Italy). *Geomorphology* **2020**, *352*, 106990.
9. Priestley, S.C.; Karlstrom, K.E.; Love, A.J.; Crossey, L.J.; Polyak, V.J.; Keppel, M.N.; Habermehl, M.A. Uranium series dating of Great Artesian Basin travertine deposits: Implications for palaeohydrogeology and palaeoclimate. *Palaeogeogr. Palaeoclimatol. Palaeoecol.* **2018**, *490*, 163–177. [[CrossRef](#)]
10. Meyer, C.M.; Aldenderfer, S.M.; Wang, Z.; Hoffmann, L.D.; Dahl, A.J.; Haas, R.W.; Schlutz, F. Permanent human occupation of the central Tibetan Plateau in the early Holocene. *Science* **2017**, *355*, 64–67. [[CrossRef](#)]
11. Liu, Z.; Li, H.; You, C.; Wan, N.; Sun, H. Thickness and stable isotopic characteristics of modern seasonal climate-controlled sub-annual travertine laminas in a travertine-depositing stream at Baishuitai, SW China: Implications for paleoclimate reconstruction. *Environ. Geol.* **2006**, *2*, 257–265. [[CrossRef](#)]
12. Filippini, L.D.; Faccenna, C.; Billi, A. Plateau versus fissure ridge travertines from Quaternary geothermal springs of Italy and Turkey: Interactions and feedbacks between fluid discharge, paleoclimate, and tectonics. *Earth Sci. Rev.* **2013**, *123*, 35–52. [[CrossRef](#)]
13. Gradzinski, M.; Wroblewski, W.; Dulinski, M. Earthquake-affected development of a travertine ridge. *Sedimentology* **2014**, *61*, 238–263. [[CrossRef](#)]
14. Wang, Z.; Yin, J. Climatic controls on travertine deposition in southern Tibet during the late Quaternary. *Palaeogeogr. Palaeoclimatol. Palaeoecol.* **2022**, *589*, 110852. [[CrossRef](#)]
15. Altunel, E.; Karabacak, V. Determination of horizontal extension from fissure-ridge travertines: A case study from the Denizli Basin, southwestern Turkey. *Geodin. Acta* **2005**, *18*, 333–342. [[CrossRef](#)]
16. Hancock, P.L.; Chalmers, R.M.L. Travertines: Using travertines in active fault studies. *J. Struct. Geol.* **1999**, *21*, 903–916. [[CrossRef](#)]
17. Williams, R.T.; Warren, D.S.; Peter, S.M. Reading a 400,000-year record of earthquake frequency for an intraplate fault. *Proc. Natl. Acad. Sci. USA* **2017**, *114*, 4893–4898. [[CrossRef](#)]
18. Karabacak, V.; Uysal, I.T.; Mutlu, H. Are U-Th Dates Correlated With Historical Records of Earthquakes? Constraints From Coseismic Carbonate Veins Within the North Anatolian Fault Zone. *Tectonics* **2019**, *7*, 2431–2448. [[CrossRef](#)]
19. Andrea, B.; Enrico, C.; Volkan, K.; Cihat, A.M.; Luo, L. Fissure Ridges: A Reappraisal of Faulting and Travertine Deposition (Travitonics). *Geosciences* **2021**, *11*, 278.
20. Matera, P.F.; Gennaro, V.; Martina, A.; Andrea, B.; Enrico, C.; Domenico, L. Geothermal fluid variation recorded by banded Ca-carbonate veins in a fault-related, fissure ridge-type travertine depositional system (Iano, southern Tuscany, Italy). *Geofluids* **2021**, *2021*, 8817487. [[CrossRef](#)]
21. Kumar, R.K.; Achutha, P.K. U-Th age evidence from carbonate veins for episodic crustal deformation of Central Anatolian Volcanic Province. *Quat. Sci. Rev.* **2017**, *177*, 158–172.
22. Andrea, B.; Enrico, C.; Riccardo, A.; Marili, B.; Mario, V. Studying travertines for neotectonics investigations: Middle–Late Pleistocene syn-tectonic travertine deposition at Serre di Rapolano (Northern Apennines, Italy). *Int. J. Earth Sci.* **2010**, *99*, 1383–1398.
23. Brogi, A.; Liotta, D.; Capezzuoli, E.; Al, E. Bagno Vignoni-Val d’Orcia area, Italy. *Geothermics* **2020**, *85*, 1–22.
24. Karabacak, V.; Ring, U.; Uysal, I.T. Earth Sciences. The off-fault deformation on the North Anatolian Fault Zone and assessment of slip rate from carbonate veins. *Chem. Chem.* **2020**, *795*, 228633.
25. Andrea, B.; Enrico, C.; Massimo, M.; Emmanuel, O.G.; Matera, P.F.; Alessandro, M. Earthquake-triggered soft-sediment deformation structures (seismites) in travertine deposits. *Tectonophysics* **2018**, *745*, 349–365.
26. Andrea, B.; Enrico, C.; Sándor, K.; Baykara, M.O.; Shen, C. Key travertine tectofacies for neotectonics and palaeoseismicity reconstruction: Effects of hydrothermal overpressured fluid injection. *J. Geol. Soc.* **2017**, *174*, 679–699.
27. Guo, Y.; Ge, Y.; Cui, P.; Chen, X.; Mao, P.; Liu, T.; Zhou, L. Early and mid-Holocene hydroclimate change recorded in tufa deposits in the Jiuzhaigou gully, eastern Tibetan Plateau. *Catena* **2021**, *196*, 278–303. [[CrossRef](#)]
28. Lv, C.; Zhao, X.; Jiang, Y.; Zhu, H.; Zhang, H.; Wang, F.; Al, E. Insights into Alpine-Karst-Type Tufa Deposits in Geological Environmental Records: A Case Study of the Calcareous Tufa Profile of the Jiuzhaigou Natural Reserve on the Eastern Margin of the Tibetan Plateau. *Minerals* **2023**, *13*, 120. [[CrossRef](#)]
29. Jiang, H.; Zhong, N.; Li, Y.; Ma, X.; Xu, H.; Shi, W.; Zhang, S.; Nie, G. A continuous 13.3-ka record of seismogenic dust events in lacustrine sediments in the eastern Tibetan Plateau. *Sci. Rep.* **2017**, *7*, 15686. [[CrossRef](#)]
30. Liang, L.; Jiang, H. Geochemical composition of the last deglacial lacustrine sediments in East Tibet and implications for provenance, weathering, and earthquake events. *Quat. Int.* **2015**, *430*, 41–51. [[CrossRef](#)]

31. Jiang, H.; Mao, X. Provenance and earthquake signature of the last deglacial Xinmocun lacustrine sediments at Diexi, East Tibet. *Geomorphology* **2014**, *204*, 518–531. [[CrossRef](#)]
32. Henck, A.; Taylor, J.; Lu, H.; Li, Y.; Yang, Q.; Grub, B.; Breslow, S. Anthropogenic hillslope terraces and swidden agriculture in Jiuzhaigou National Park, northern Sichuan, China. *Quat. Res.* **2009**, *73*, 201–207. [[CrossRef](#)]
33. Zhang, H.; Zhao, X.; Wang, F.; Wu, C.; Li, S. Radioactivity of Nuorilang waterfall travertine dam in Jiuzhaigou valley, Sichuan Province and its implication for the sedimentary environment. *Carsologica Sin.* **2021**, *40*, 157–165. [[CrossRef](#)]
34. Dong, F.; Dai, Q.; Rao, H.; Wang, F.; Zhao, X.; Enrico, C.; Augusto, A. Comparative study on microbial deposition of travertine in Huanglong scenic area and Yellowstone National Park. *Carsologica Sin.* **2021**, *40*, 264–272. [[CrossRef](#)]
35. Gan, J. A System Study on the Geological Environment and Water Cycle at the Jiuzhaigou Valley. Master's Thesis, Southwest Jiaotong University, Chengdu, China, 2007.
36. Team, S. *1:50,000 Ecological Geology Map and Report of Jiuzhaigou*; Geological Publishing House: Beijing, China, 2000; pp. 1–140.
37. Qiao, X.; Xiao, Y.; Du, J.; Tang, Y.; Xiao, W.; Zhang, X.; Zhang, M. Tufa Landscapes in the Key Scenic Areas of the Jiuzhaigou Natural World Heritage Site: A critical Review and Future Research Needs. *Earth Environ.* **2022**, *50*, 202–218.
38. Peng, D.; Xie, Y.X. Multiple stratigraphic classification and correlation of the Devonian- Triassic in the Jiuzhaigou area, Sichuan, and its sedimentary environment. *Geol. China* **2006**, *33*, 1013e–1022e.
39. Xinlei, Z.; Ya, T.; Du, J.; Stefano, L.; Yao, X.; Qingxia, Y.; Hailiang, S.; Xue, Q. Enhanced soil erosion threatens fluvial tufa landscapes after an Ms. 7.0 earthquake in the Jiuzhaigou World Heritage Site, southwestern China. *Sci. Total Environ.* **2022**, *848*, 157632.
40. Zhao, B.; Xu, W.Y. Background and reflections on Dingxi earthquake of July 22, 2013. *Nat. Hazards* **2014**, *70*, 1661–1667. [[CrossRef](#)]
41. Zhang, K. Is the Songpan-Ganzi terrane (central China) really underlain by oceanic crust? *J. Geol. Soc. India* **2001**, *57*, 223–230.
42. Zhang, P.; Wen, X.; Shen, Z.; Chen, J. Oblique, high-angle, listric-reverse faulting and associated development of strain: The Wenchuan earthquake of May 12, 2008, Sichuan, China. *Annu. Rev. Earth Pl. Sc.* **2010**, *38*, 353–382. [[CrossRef](#)]
43. Hao, L.; Xiuling, W.; Hang, H.; Linjian, S.; Deqiang, Y.; Hao, W. The earthquake in Jiuzhaigou County of Northern Sichuan, China on August 8, 2017. *Nat. Hazards* **2018**, *90*, 1021–1030.
44. Wei, X.; Chen, G.; Kun, R.; Xu, C.; Yu, W.; Qi, L. Discussion on seismogenic structure of Jiuzhaigou earthquake and its implication for current strain state in the southeastern Qinghai-Tibet Plateau. *Chin. J. Geophys.* **2017**, *10*, 4018–4026.
45. Dai, L.; Fan, X.; Jansen, J.D. Landslides and fluvial response to landsliding induced by the 1933 Diexi earthquake, Minjiang River, eastern Tibetan Plateau. *Landslides* **2021**, *18*, 3011–3025. [[CrossRef](#)]
46. Feng, J.; Chen, L.; Han, M.; Gao, S.; Li, Y.; Lu, L.; Chen, S. Multi-fault rupture behavior of the 1786 M 7.3/4 Kangding earthquake on the eastern margin of the Tibetan Plateau. *Front. Earth Sci.* **2023**, *11*, 1140326. [[CrossRef](#)]
47. Li, H.; Deng, Z.; Chen, L. Simulation study on the influencing factors of surface rupture zone distribution of strike-slip fault: take Luhuo MS7.6 earthquake in 1973 for example. *Chin. J. Geophys.* **2019**, *8*, 2871–2884.
48. Yue, H.; Zhang, Z.; Chen, Y. Interaction between adjacent left-lateral strike-slip faults and thrust faults: The 1976 Songpan earthquake sequence. *Chin. Sci. Bull.* **2008**, *53*, 2520–2526. [[CrossRef](#)]
49. Niu, A.; Zhang, L.; Yan, W.; Jia, X.; Li, X. On the Characteristics of Ground Deformation Anomalies in the Middle and Northern Part of the South-North Seismic Belt prior to the Wenchuan Earthquake. *Earthquake* **2009**, *1*, 100–107.
50. Wang, L.; Chen, S.; Zhuang, J.; Zhang, B.; Shi, W.; Yang, J.; Xu, W. Gravity field changes reveal deep mass transfer before and after the 2013 Lushan earthquake. *Commun. Earth Environ.* **2023**, *4*, 194. [[CrossRef](#)]
51. Lu, J.; Xiang, S.; Jiang, S.; Liu, C.; Zeng, F. Analysis of Soil Granularity at Dazhuka Country, Rikeze. *J. Arid. Land Resour. Environ.* **2008**, *22*, 80–85. [[CrossRef](#)]
52. Wang, J. Response of Stream Geomorphic Indices and Lacustrine Sediments to the Activity of Daqingshan Piedmont Fault. Master's Thesis, National Institute of Natural Hazards, MEMC, Beijing, China, 2021.
53. Mao, X. Preliminary Study on Lacustrine Sediments at Diexi in the Upper Reach of the Minjiang River during the last deglaciation. Master's Thesis, China University of Geosciences, Beijing, China, 2011.
54. Václav, S.; Pachnerová, B.K.; Zachariáš, J.; Světlík, L.; Borecká, L. Gothic-Arch Calcite from Speleothems of the Bohemian Karst (Czech Republic): Its Occurrence, Microscopic Ultrastructure and Possible Mechanism of Growth. *Minerals* **2021**, *11*, 866.
55. LI, B.; Sun, G.; Zhong, H.; LI, S.; Wang, Y.; Zhao, L.; LI, X. Rare Earth Element Characteristics of Surface Sediments in the Fujian Coastal Area and their Implications for Provenance. *Mar. Geol. Front.* **2017**, *33*, 47–56. [[CrossRef](#)]
56. Guo, M.; Xu, L. Geochemical Features of Rare Earth Elements in Sediments of the Chaohu Lake and its Environmental Implications. *Mar. Geol. Quat. Geol.* **2016**, *36*, 137–144. [[CrossRef](#)]
57. Wu, S.; Yang, H.; Fan, H.; Xia, Y.; Meng, Q.; He, S.; Gong, X. Assessment of the Effect of Organic Matter on Rare Earth Elements and Yttrium Using the Zhijin Early Cambrian Phosphorite as an Example. *Minerals* **2022**, *12*, 876. [[CrossRef](#)]
58. Committee, S.P.L.C. *Annals of Sichuan Province*; Sichuan People's Publishing House: Chengdu, China, 1998; pp. 1–379.
59. Jibson, R.W. A Public Health Issue Related To Collateral Seismic Hazards: The Valley Fever Outbreak Triggered By The 1994 Northridge, California Earthquake. *Surv. Geophys.* **2002**, *23*, 511–528. [[CrossRef](#)]
60. Tang, C.; Zhu, J.; Li, W.; Liang, J. Rainfall-triggered debris flows following the Wenchuan earthquake. *Bull Eng. Geol. Environ.* **2009**, *68*, 187–194. [[CrossRef](#)]
61. Wang, F.; Dong, F.; Zhao, X.; Sun, S.; Dai, Q.; Li, Q. The large dendritic fissures of travertine dam exposed by Jiuzhaigou earthquake, Sichuan, southwestern China. *Int. J. Earth Sci.* **2018**, *107*, 2785–2786. [[CrossRef](#)]

62. Stefano, L.; Tang, Y.; Matteo, R.; Qiao, X.; Schreiber, B.C.; Deng, G. Seasonal Pattern In the High-Elevation Fluvial Travertine From the Jiuzhaigou National Nature Reserve, Sichuan, Southwestern China. *J. Sediment. Res.* **2017**, *87*, 253–271.
63. Wen, X.; Wu, Y.; Huang, C.; Luo, M.; Chen, K. Grain size & elements composition characteristics and their Implications for provenance of the late pleistocene loess in the upper reaches of the minjiang river china. *Mt. Res.* **2019**, *37*, 488–498. [[CrossRef](#)]
64. Jiang, H.; Zhong, N.; Li, Y.; Xu, H.; Ma, X.; Meng, Y.; Mao, X. Magnetostratigraphy and grain size record of the Xijiadian fluviolacustrine sediments in East China and its implied stepwise enhancement of the westerly circulation during the Eocene period. *J. Geophys. Res. Solid Earth* **2014**, *119*, 7442–7457. [[CrossRef](#)]
65. Pye, K.; Tsoar, H. The mechanics and geological implications of dust transport and deposition in deserts with particular reference to loess formation and dune sand diagenesis in the northern Negev, Israel. *Geol. Soc. Lond. Spec. Publ.* **1987**, *35*, 139–156. [[CrossRef](#)]
66. Lu, H.; An, Z. Comparison of Grain-size Distribution of Red Clay and Loess-paleosol Deposits in Chinese Loess Plateau. *Acta Sedimentol. Sin.* **1999**, *17*, 226–232.
67. Yu, X.; Zhou, W.; Liu, X. Grain size characteristics of the holocene peat sediment in eastern Tibetan plateau and its paleo—climatic significance. *Acta Sedimentol. Sin.* **2006**, *24*, 64–869.
68. Zhang, K.; Li, Q.; Yan, L.; Lu, L.; Zhang, Y.; Hui, J.; Tang, X. Geochemistry of limestones deposited in various plate tectonic settings. *Earth Sci. Rev. Int. Geol. J. Bridg. Gap Between Res. Artic. Textb.* **2017**, *167*, 27–46. [[CrossRef](#)]

**Disclaimer/Publisher’s Note:** The statements, opinions and data contained in all publications are solely those of the individual author(s) and contributor(s) and not of MDPI and/or the editor(s). MDPI and/or the editor(s) disclaim responsibility for any injury to people or property resulting from any ideas, methods, instructions or products referred to in the content.